

# SHAMISA: SHAPed Modeling of Implicit Structural Associations for Self-supervised No-Reference Image Quality Assessment

Mahdi Naseri and Zhou Wang

**Abstract**—No-Reference Image Quality Assessment (NR-IQA) aims to estimate perceptual quality without access to a reference image of pristine quality. Learning an NR-IQA model faces a fundamental bottleneck: its need for a large number of costly human perceptual labels. We propose SHAMISA, a non-contrastive self-supervised framework that learns from unlabeled distorted images by leveraging explicitly structured relational supervision. Unlike prior methods that impose rigid, binary similarity constraints, SHAMISA introduces implicit structural associations, defined as soft, controllable relations that are both distortion-aware and content-sensitive, inferred from synthetic metadata and intrinsic feature structure. A key innovation is our compositional distortion engine, which generates an uncountable family of degradations from continuous parameter spaces, grouped so that only one distortion factor varies at a time. This enables fine-grained control over representational similarity during training: images with shared distortion patterns are pulled together in the embedding space, while severity variations produce structured, predictable shifts. We integrate these insights via dual-source relation graphs that encode both known degradation profiles and emergent structural affinities to guide the learning process throughout training. A convolutional encoder is trained under this supervision and then frozen for inference, with quality prediction performed by a linear regressor on its features. Extensive experiments on synthetic, authentic, and cross-dataset NR-IQA benchmarks demonstrate that SHAMISA achieves strong overall performance with improved cross-dataset generalization and robustness, all without human quality annotations or contrastive losses.

**Index Terms**—blind image quality assessment, self-supervised learning, graph-based representation learning, distortion modeling, perceptual quality prediction

## I. INTRODUCTION

**I**MAGE Quality Assessment (IQA) aims to estimate perceptual image quality in line with human opinion. The No-Reference setting (NR-IQA) is especially challenging, as it must operate without reference images or distortion labels. NR-IQA is critical for real-world tasks such as perceptual enhancement [1], image captioning [2], and streaming optimization [3]. However, modeling perceptual quality is difficult due to the complex interplay between distortion types and content [4], [5]. Supervised approaches [6]–[8] rely on extensive human annotations, with KADID-10K [9] alone requiring over 300,000 subjective ratings, making them expensive and

hard to scale. To address this, recent efforts turn to self-supervised learning (SSL), using unlabeled distorted images to learn quality-aware representations [10], [11], typically via contrastive objectives tailored to either content or degradation similarity.

Classical SSL methods like SimCLR [12] and MoCo [13], developed for classification, learn content-centric and distortion-invariant features. Such representations misalign with NR-IQA, where both content and degradation must be modeled. To bridge this gap, contrastive SSL-IQA methods introduce domain-specific objectives but can suffer from sampling bias because sampled negatives may include semantically related false negatives [14]–[16]. CONTRIQUE [17] groups images by distortion type and severity, ignoring content. Re-IQA [11], by contrast, uses overlapping crops of the same image to promote content-aware alignment. While each mode captures useful relations, similarity is enforced either across content or across distortions, but not both. This leads to scattered embeddings for similarly degraded images with different content [18]. ARNIQA [18] learns a distortion manifold by aligning representations of similarly degraded images, irrespective of content. Yet, such approaches rigidly collapse embeddings without accounting for perceptual effects like masking [4], where content alters perceived quality. In practice, perceptual similarity depends jointly on both distortion severity and image content, a dependency that current SSL-IQA models fail to capture in a flexible, scalable manner.

We propose **SHAMISA** (SHAPed Modeling of Implicit Structural Associations), a non-contrastive self-supervised framework that addresses this challenge by learning representations jointly sensitive to both distortion and content through explicitly constructed relation graphs. “SHAPed Modeling” refers to graph-based relational supervision, whereas “Implicit Structural Associations” denote the latent perceptual relations encoded in these graphs, providing finer control over similarity learning than prior SSL-IQA methods that treat distorted views uniformly. SHAMISA draws inspiration from ExGRG [19], which introduced explicit graph-based guidance for self-supervised learning in the graph domain. In contrast, SHAMISA extends this idea to visual data, where quality prediction depends on fine-grained perceptual variations. Prior methods implicitly impose sparse relational structures, resulting in disconnected or inconsistent supervision, which SHAMISA addresses through explicitly shaped relation graphs.

At the core of SHAMISA is a compositional distortion

Mahdi Naseri and Zhou Wang are with the Department of Electrical and Computer Engineering, University of Waterloo, Waterloo, ON N2L 3G1, Canada (e-mail: mahdi.naseri@uwaterloo.ca; zhou.wang@uwaterloo.ca). Corresponding author: Mahdi Naseri.

engine that generates infinite compositional degradations from continuous parameter spaces. Each mini-batch is built from reference images that form distortion composition groups where only one degradation factor varies, enabling controlled sampling across content, distortion type, and severity. From this, we build two categories of relation graphs: (i) **Metadata-Driven Graphs**, which encode pairwise similarity based on distortion metadata, encouraging images with similar degradations to lie close in the learned manifold while inducing controlled representational shifts as distortion severity varies; and (ii) **Structurally Intrinsic Graphs**, constructed from the latent feature space using  $k$ -nearest neighbors (kNN) and deep clustering. These graphs supervise a non-contrastive VICReg-style objective, optimized in a single update that constructs relation graphs from the current representations and applies stop-gradient through graph construction.

SHAMISA unifies content-dependent and distortion-dependent learning within a single relational framework, generalizing the rigid pairing schemes used in prior SSL-IQA methods. At test time, the learned encoder is frozen and paired with a linear regressor to predict quality scores. SHAMISA achieves strong performance across both synthetic and authentic datasets without requiring human quality labels or contrastive objectives.

Our main contributions are:

- 1) We introduce **SHAMISA**, a non-contrastive self-supervised framework for NR-IQA that encodes both distortion-aware and content-aware information into a shared representation space via explicit relational supervision.
- 2) We propose a distortion engine that generates compositional groups with controlled variation, enabling fine-grained similarity learning across distortion factors and content.
- 3) We develop a dual-source relation graph construction strategy that combines Metadata-Driven Graphs based on known degradation metadata and Structurally Intrinsic Graphs derived from the evolving feature space, trained with a stop-gradient alternating update that couples on-the-fly graph construction with representation learning.
- 4) SHAMISA generalizes the rigid pairing schemes used in prior SSL-IQA methods within a unified graph-weighted invariance framework and achieves strong overall performance across synthetic, authentic, and cross-dataset benchmarks, including the strongest overall six-dataset average among the compared SSL methods, together with improved robustness and transfer.

## II. RELATED WORK

### A. Traditional and Supervised NR-IQA

No-Reference Image Quality Assessment (NR-IQA) aims to estimate perceptual image quality without access to pristine references. Traditional methods rely on handcrafted features derived from Natural Scene Statistics (NSS), modeling distortions as deviations from expected regularities. Examples

include BRISQUE [20], NIQE [21], DIIVINE [22], and BLI-INDS [23], while CORNIA [24] and HOSA [25] construct codebooks from local patches. Though effective on synthetic distortions, these models often fail on authentically distorted images due to a lack of semantic awareness.

Supervised NR-IQA models typically use pre-trained CNNs (e.g., ResNet [26]) to extract deep features, which are mapped to quality scores via regression. Techniques like HyperIQA [7], RAPIQUE [27], and MUSIQ [28] adapt neural architectures for perceptual modeling. PaQ-2-PiQ [29] incorporates both image- and patch-level quality labels. Others like DB-CNN [6] and PQR [30] combine multiple feature streams. However, such methods require large-scale and costly human annotations, limiting scalability and generalization.

### B. Self-Supervised Learning for NR-IQA

Self-supervised learning (SSL) enables representation learning from unlabeled data. Contrastive methods like SimCLR [12] and MoCo [13] rely on sampled negatives, which can introduce false negatives and sampling bias when semantically related samples are treated as negatives [14]–[16]. Non-contrastive methods like VICReg [31] avoid negatives through invariance and decorrelation. In graph domains, ExGRG [19] introduces explicit relation graphs for SSL, combining domain priors and feature structure. SHAMISA adopts a similar inductive bias but applies it to NR-IQA, where perceptual similarity depends jointly on content and degradation.

Recent SSL-IQA works adapt these paradigms to quality prediction. CONTRIQUE [17] clusters samples with similar distortion types into classes, learning quality-aware embeddings. QPT [10] aligns patches under shared distortion assumptions. Re-IQA [11] uses two encoders: one pre-trained for content-specific features and another trained for distortion-specific features. Their outputs are concatenated and fed to a single linear regressor. This assumes that a shallow fusion layer can recover complex content-distortion interactions from separately learned streams. Re-IQA may therefore under-represent content-distortion interactions, even though these interactions play a central role in perceptual quality assessment rather than being evaluated in isolation [32], [33].

ARNIQA [18] instead aligns representations of images degraded equally, disregarding content. While it captures distortion similarity, it rigidly enforces uniform proximity and ignores perceptual effects introduced by content. In contrast, SHAMISA learns a unified representation space that respects both distortion and semantic structure, using two complementary relation graphs. A metadata-driven graph and a structurally intrinsic graph together encode distortion-aware similarity and perceptual affinities across content. This provides soft, fine-grained constraints that generalize prior methods as special cases.

### C. Compositional Distortion Modeling and Relational Supervision

Degradation engines are central to SSL-IQA training. Prior models apply a limited set of discrete distortions or fixed composition rules [10], [11]. ARNIQA, for example, applies

sequential distortions with fixed sampling schemes but lacks structured sampling for controlled variation. RealESRGAN [1] follows a fixed distortion sequence from predefined groups. Such engines offer limited degradation diversity and do not support relational supervision.

SHAMISA introduces a compositional distortion engine that generates continuously parameterized degradations with uncountable variation. We partition each mini-batch into *tiny-batches* (small, fixed-size subsets). Each tiny-batch contains distortion composition groups in which only one degradation factor varies, enabling precise control over severity and type. This supports precise metadata generation for graph construction. Unlike prior works that enforce binary or fixed similarity constraints, SHAMISA enables structured shifts in representation space by applying soft supervision from graph relations. Similar samples lie closer, while severity variation introduces gradual transitions.

Combined with its dual-graph relational supervision, SHAMISA learns distortion-aware, content-sensitive embeddings in a non-contrastive setting. By decoupling quality learning from rigid class labels and negative sampling, SHAMISA offers a scalable and generalizable framework for NR-IQA without relying on human quality annotations or conventional augmentation heuristics.

### III. METHOD

As illustrated in Fig. 1, SHAMISA combines structured distortion generation with dual-source relational supervision to learn quality-aware features in a non-contrastive setting. We then transfer the learned encoder to NR-IQA by freezing backbone representations and fitting a lightweight regressor, so downstream performance reflects representation quality rather than head complexity.

#### A. Overview and SSL Formulation for NR-IQA

We pre-train a ResNet-50 encoder  $f_\theta$  with a 2-layer MLP projector  $g_\psi$  on unlabeled images degraded online by our distortion engine, optimizing a VICReg-style non-contrastive objective [31] to avoid negative sampling and its sampling-bias issues [14]. After this self-supervised pre-training, we discard  $g_\psi$ , freeze  $f_\theta$  (never fine-tune), and train a linear regressor on the frozen features for quality prediction.

*a) Tensorized batch construction:* Let  $N_{\text{ref}}$  denote the number of reference images per mini-batch and  $N_{\text{comp}}$  the number of distortion compositions applied to each reference image (Sec. III-B). We take *one* random crop per pristine image to form

$$\mathbf{R}^s \in \mathbb{R}^{N_{\text{ref}} \times 3 \times H_{in} \times W_{in}}.$$

Sampling  $N_{\text{comp}}$  compositions  $\{\chi_d\}_{d=1}^{N_{\text{comp}}}$  yields distorted sets

$$\mathbf{X}^{(d)} = \chi_d(\mathbf{R}^s) \in \mathbb{R}^{N_{\text{ref}} \times 3 \times H_{in} \times W_{in}}, \quad d = 1, \dots, N_{\text{comp}}.$$

We concatenate references and all distorted sets:

$$\mathbf{X} = [\mathbf{R}^s; \mathbf{X}^{(1)}; \dots; \mathbf{X}^{(N_{\text{comp}})}] \in \mathbb{R}^{N \times 3 \times H_{in} \times W_{in}}, \quad (1)$$

$$N = N_{\text{ref}}(N_{\text{comp}} + 1).$$

Representations  $\mathbf{H}$  and Embeddings  $\mathbf{Z}$  are

$$\mathbf{H} = f_\theta(\mathbf{X}) \in \mathbb{R}^{N \times d_h}, \quad \mathbf{Z} = g_\psi(\mathbf{H}) \in \mathbb{R}^{N \times d_z}.$$

Human opinion scores are used only for the regression head after pre-training.

#### B. Compositional Distortion Engine

A *distortion function* is one atomic degradation from KADID-10K with 24 functions across 7 categories (Brightness change, Blur, Spatial, Noise, Color, Compression, Sharpness & Contrast) [9]. A *distortion composition* in SHAMISA is an *ordered composition* of multiple distortion functions with at most one function per category, applied sequentially. Unlike prior SSL-IQA setups based on discrete severity grids [10], [18], SHAMISA samples *continuous* severities, yielding an *uncountable* family of compositions. Order is perceptually consequential, hence we randomize it. In practice each iteration uses a finite  $N_{\text{comp}}$ , but randomization across iterations explores novel compositions, and continuous level differences are exploited later by our relation graphs.

*a) Severity calibration:* For each distortion function  $f_m$  we map its native parameter domain  $[\lambda_m^{\min}, \lambda_m^{\max}]$  into  $[0, 1]$  via a piecewise-linear calibration  $\rho_m : [\lambda_m^{\min}, \lambda_m^{\max}] \rightarrow [0, 1]$  obtained by linearly interpolating the discrete intensities used in [9]. This yields comparable per-function normalized severities. During sampling we operate in the normalized space; if needed, we recover native parameters by  $\rho_m^{-1}$ .

*b) Sampling a composition:* For each distortion composition we sample a tuple  $(M, S, f, \pi, \lambda)$  where:  $M \sim \text{Unif}\{1, \dots, M_d\}$  is the number of distortion functions in the composition with at most one per category;  $S \subset \{1, \dots, 7\}$  is a size- $M$  subset indexing the seven KADID-10K distortion categories, sampled uniformly without replacement;  $f = (f_1, \dots, f_M)$  picks one function per category in  $S$ ;  $\pi$  is a permutation of  $\{1, \dots, M\}$  sampled uniformly indicating the application order; and  $\lambda = (\lambda_1, \dots, \lambda_M) \in [0, 1]^M$  are per-function normalized severities sampled i.i.d. by drawing  $\epsilon_m \sim \mathcal{N}(0, 0.5^2)$  and setting  $\lambda_m = \min(1, |\epsilon_m|)$ , where  $[0, 1]^M$  is the  $M$ -dimensional unit hypercube. Given an input image  $x$ , let  $\theta_m := \rho_m^{-1}(\lambda_m)$  and write  $f_m(\cdot; \theta_m)$ . The composed degradation is

$$\mathcal{C}(x; \pi, f, \lambda) = (f_{\pi(M)}(\cdot; \theta_{\pi(M)}) \circ \dots \circ f_{\pi(1)}(\cdot; \theta_{\pi(1)}))(x). \quad (2)$$

*1) Single-factor variation and trajectories:* Each mini-batch is partitioned into  $B$  tiny-batches; we use  $[n] := \{1, \dots, n\}$  for index ranges, so  $i \in [B]$  indexes tiny-batches. In tiny-batch  $i$ , select  $R$  references  $\{r_{i,j}\}_{j=1}^R$  and instantiate  $C$  distortion composition groups. For the  $k$ -th composition group ( $k \in [C]$ ), sample a base composition  $(M_{i,k}, S_{i,k}, f_{i,k}, \pi_{i,k}, \lambda_{i,k}^{(0)})$ , where  $\lambda_{i,k}^{(0)} \in [0, 1]^{M_{i,k}}$  is the base severity vector. Choose exactly one *varying coordinate*  $m^*(i, k) \in \{1, \dots, M_{i,k}\}$ , that is, exactly one distortion function whose level will vary within the composition group, and generate  $L$  severity levels  $\{s_{i,k}^{(l)}\}_{l=1}^L \subset [0, 1]$ . We draw

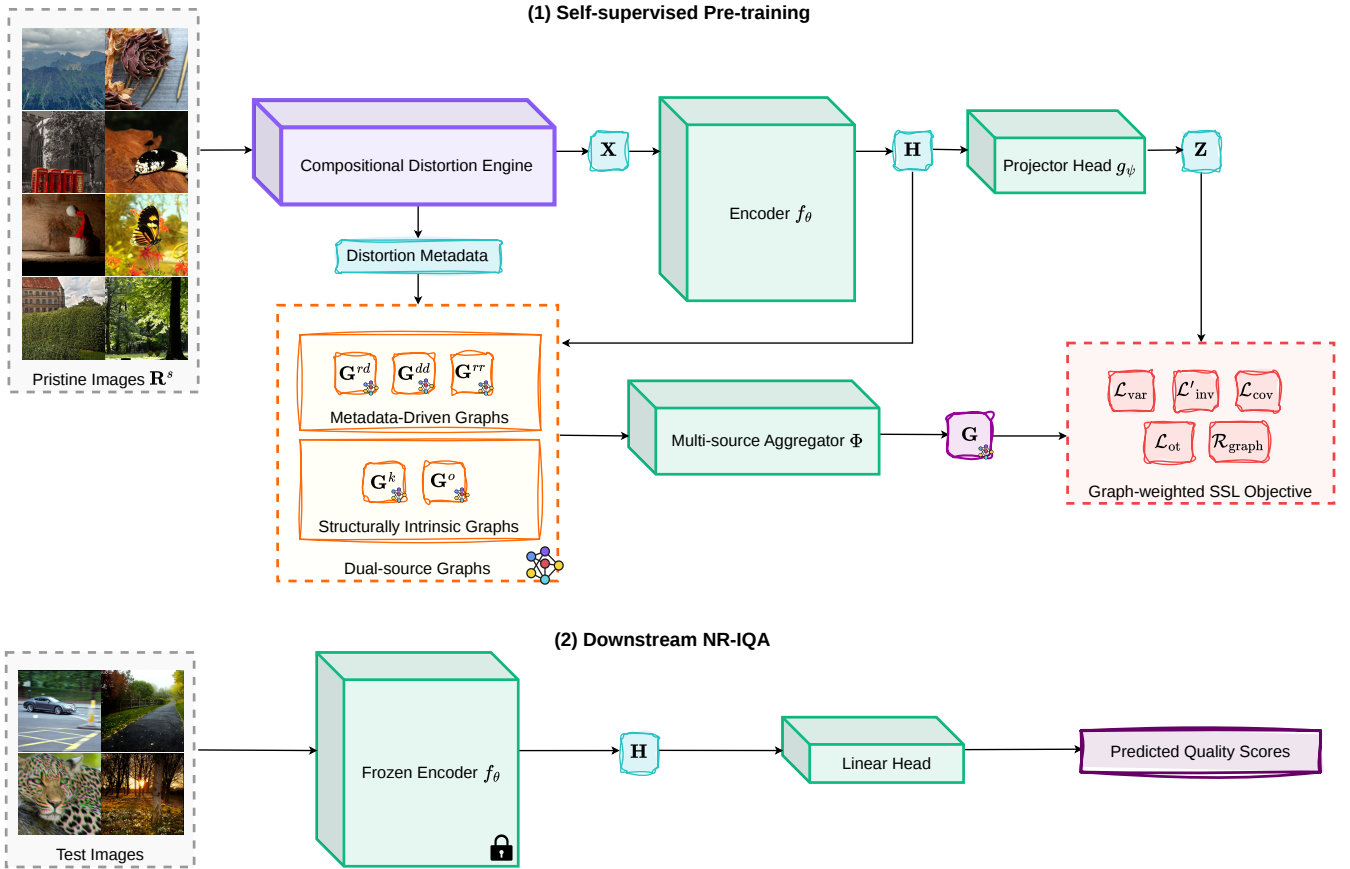


Fig. 1. **Overview of the proposed SHAMISA framework.** (1) **Self-supervised pre-training:** pristine images are transformed by a compositional distortion engine to form a mini-batch  $\mathbf{X}$  and distortion metadata; the encoder  $f_\theta$  and projector  $g_\psi$  produce representations  $\mathbf{H}$  and embeddings  $\mathbf{Z}$  used to construct dual-source relation graphs (metadata-driven and structurally intrinsic), which are aggregated by a multi-source aggregator  $\Phi$  into  $\mathbf{G}$  and optimize a graph-weighted SSL objective. (2) **Downstream NR-IQA:** we freeze  $f_\theta$  and train a lightweight regressor on top of  $\mathbf{H}$  to predict quality scores.

each level i.i.d. as  $s_{i,k}^{(l)} = \min(1, |\epsilon^{(l)}|)$  with  $\epsilon^{(l)} \sim \mathcal{N}(0, 0.5^2)$ . Define the per-level severities component-wise by

$$(\lambda_{i,k}^{(l)})_m = \begin{cases} (\lambda_{i,k}^{(0)})_m, & m \neq m^*(i, k), \\ s_{i,k}^{(l)}, & m = m^*(i, k). \end{cases}$$

This single-factor scheme varies one distortion function while holding the others fixed, producing controlled severity variation that isolates that function's effect in the learned representation. Formally, applying the level- $l$  composition in group  $k$  to reference  $r_{i,j}$  yields the distorted image

$$x_{i,j,k,l} = \mathcal{C}(r_{i,j}; \pi_{i,k}, f_{i,k}, \lambda_{i,k}^{(l)}), \quad i \in [B], j \in [R], k \in [C], l \in [L]. \quad (3)$$

Consequently, the mini-batch contains  $N_{\text{ref}} = BR$  references and each reference receives  $N_{\text{comp}} = CL$  compositions, with sampling performed independently for each tiny-batch.

### C. Explicit Relation Graphs and Graph-weighted VICReg

We adopt the variance and covariance regularizers of VICReg [31] and replace its augmentation-paired invariance term

$\mathcal{L}_{\text{inv}}$  with a graph-weighted variant  $\mathcal{L}'_{\text{inv}}$ , in the spirit of explicitly generated relation graphs [19]:

$$\mathcal{L}_{\text{var}} = \sum_{t=1}^{d_z} \max(0, 1 - \sqrt{\text{Cov}(\mathbf{Z})_{t,t}}), \quad (4)$$

$$\mathcal{L}_{\text{cov}} = \sum_{t=1}^{d_z} \sum_{\substack{u=1 \\ u \neq t}}^{d_z} \text{Cov}(\mathbf{Z})_{t,u}^2, \quad (5)$$

$$\mathcal{L}_{\text{inv}} = \sum_{(i,j) \in \mathcal{A}} \|\mathbf{z}_{i,\cdot} - \mathbf{z}_{j,\cdot}\|_2^2, \quad (6)$$

$$\mathcal{L}'_{\text{inv}} = \sum_{i=1}^N \sum_{j=1}^N \mathbf{G}_{i,j} \|\mathbf{z}_{i,\cdot} - \mathbf{z}_{j,\cdot}\|_2^2. \quad (7)$$

Here  $\mathcal{A} \subseteq [N] \times [N]$  denotes the set of augmentation positives, and  $\mathbf{G} \in [0, 1]^{N \times N}$  is the weighted adjacency matrix of a soft relation graph (Sec. III-F), where each entry specifies how strongly the corresponding pair is encouraged to remain invariant. These soft, controllable entries of  $\mathbf{G}$  instantiate the implicit structural associations, encoding relational cues that jointly capture content and distortion. Intuitively,  $\mathcal{L}_{\text{var}}$  enforces a minimum per-dimension variance to avoid collapse,  $\mathcal{L}_{\text{cov}}$  decorrelates dimensions, and  $\mathcal{L}'_{\text{inv}}$  brings together embeddings proportionally to relational strengths encoded by  $\mathbf{G}$ . In contrast,  $\mathcal{L}_{\text{inv}}$  uses a *rigid* binary set  $\mathcal{A}$  of augmentation positives.

When  $\mathbf{G}$  is the binary indicator of  $\mathcal{A}$  (i.e.,  $\mathbf{G}_{i,j} = 1$  iff  $(i,j) \in \mathcal{A}$  and 0 otherwise), Eq. 7 reduces to VICReg’s original invariance in Eq. 6.

Our self-supervised pre-training objective is

$$\mathcal{L}_{\text{ssl}} = \alpha \mathcal{L}_{\text{var}} + \beta \mathcal{L}_{\text{cov}} + \gamma \mathcal{L}'_{\text{inv}}. \quad (8)$$

SHAMISA remains *non-contrastive*: we do not use negatives and instead prevent collapse via the variance-covariance terms [31], rather than through negative pairs as in contrastive methods [12].

*a) Relation to prior positives:* Cosine invariance underlies InfoNCE in SimCLR [12]. With  $\ell_2$ -normalized features,  $\|a - b\|_2^2 = 2(1 - \cos(a, b))$ , so Euclidean and cosine invariances are equivalent up to scaling. Thus, prior invariances that rely on *rigid binary pairings* become special cases of SHAMISA’s *soft* graph-weighted invariance. ARNIQA pairs images with the same distortion type and level across different contents [18]; Re-IQA pairs overlapping crops of the same image (content-driven) [11]; CONTRIQUE uses synthetic distortion classes or instance discrimination for UGC [10], [17]. Each choice is recovered by setting  $\mathbf{G}$  to the corresponding sparse binary adjacency.

*b) Why an explicit  $\mathbf{G}$ ? Laplacian Eigenmap view:* In two-view augmentation setups, the augmentation graph splits into exactly  $N/2$  disconnected components, so its Laplacian has  $N/2$  zero eigenvalues [34]. Allowing soft cross-component edges in  $\mathbf{G}$  alleviates this rank deficiency and yields a better posed invariance term [19]. *Alternating update view:* We construct  $\mathbf{G}$  from the current representations to define soft relational targets, then update  $f_\theta$  and  $g_\psi$  by minimizing Eq. 8. A stop-gradient on the graph inputs, defined formally in Sec. III-F, lets graph construction and parameter updates be executed in a single optimization step [19], [35].

#### D. Metadata-Driven Graphs

We convert engine metadata into soft relational weights that shape the embedding space through two complementary effects. Within a given content, similarity to the pristine anchor decreases smoothly as severity increases. Across contents, samples from the same distortion composition group remain neighbors when their severities are close.

We next define two monotone maps  $\phi, \hat{\phi} : [0, 1] \rightarrow [0, 1]$ , with  $\phi'(u) \leq 0$  and  $\hat{\phi}'(u) \leq 0$ , that convert a normalized severity or severity gap into a similarity weight. For simplicity, we set  $\phi(u) = \hat{\phi}(u) = \exp(-\kappa u)$ ; both maps are bounded in  $[0, 1]$  and strictly decreasing in  $u$ .

*1) Reference-distorted graph  $\mathbf{G}^{rd}$ :* Recall that in tiny-batch  $i$  and group  $k$ ,  $m^*(i, k)$  is the varying function and  $\lambda_{i,k}^{(l)} \in [0, 1]^{M_{i,k}}$  is the level- $l$  severity vector. We assign an edge from each reference to *each* of its degraded versions:

$$\mathbf{G}^{rd}[r_{i,j}, x_{i,j,k,l}] = \phi\left(\left(\lambda_{i,k}^{(l)}\right)_{m^*(i,k)}\right). \quad (9)$$

*Intuition.* Small severities yield  $\phi \approx 1$  and keep mild degradations near the pristine anchor; large severities drive  $\phi \rightarrow 0$ , allowing strong degradations to move away. This produces smooth, severity-aware attraction without collapse.

*2) Distorted-distorted graph  $\mathbf{G}^{dd}$ :* Within the same distortion composition group  $(i, k)$ , define the 1D severity gap

$$\delta_{i,k}(l, l') = |s_{i,k}^{(l)} - s_{i,k}^{(l')}| \in [0, 1],$$

and, for any  $j, j' \in [R]$ , define the edge weight between two distorted images whose contents may differ as

$$\mathbf{G}^{dd}[x_{i,j,k,l}, x_{i,j',k,l'}] = \hat{\phi}\left(\delta_{i,k}(l, l')\right). \quad (10)$$

*Intuition.* Nearby severity levels attract; distant levels do not. This ties together similarly degraded images *regardless of content*, complementing  $\mathbf{G}^{rd}$ . To avoid density, we apply a *global* Top- $K_d$  sparsifier:

$$\mathbf{G}^{dd} \leftarrow F_{K_d}(\mathbf{G}^{dd}),$$

where  $F_{K_d}$  retains the  $K_d$  largest entries *in the whole matrix* and zeros the rest.

*3) Reference-reference graph  $\mathbf{G}^{rr}$ :* We weakly connect pristine images across contents to stabilize a common high-quality anchor:

$$\mathbf{G}^{rr}[r_{i,j}, r_{i',j'}] = w_{rr}, \quad w_{rr} \in (0, 1]. \quad (11)$$

*Intuition.* This graph builds a coherent pristine neighborhood across contents without forcing content collapse; variance-covariance regularizers prevent trivial solutions while these links stabilize a shared high-quality anchor in the representation space.

The three metadata graphs provide *severity-aware, content-aware* soft relations that are fed to the overall relation aggregation (Sec. III-F) and used inside the graph-weighted invariance term (Eq. 7) to shape quality-sensitive embeddings.

#### E. Structurally Intrinsic Graphs

Beyond metadata, we inject *emergent* structure from the evolving representation space. These graphs encourage local manifold smoothness and global prototype organization, complementing the metadata graphs.

*1) kNN relation graph:* Compute cosine similarities on encoder features  $\mathbf{H}$ :

$$\mathbf{S}_{i,j}^H = \frac{\mathbf{H}_{i,\cdot}^\top \mathbf{H}_{j,\cdot}}{\|\mathbf{H}_{i,\cdot}\|_2 \|\mathbf{H}_{j,\cdot}\|_2}.$$

Form the kNN graph by keeping, for each sample, the top  $k_n$  similarity scores and removing self-connections:

$$\mathbf{G}^k = F_{k_n}(\mathbf{S}^H) \in \mathbb{R}^{N \times N}, \quad (12)$$

where  $F_{k_n}$  retains the largest  $k_n$  entries in each row of  $\mathbf{S}^H$  and zeros the rest.

*Intuition.* Deep features are well correlated with perceptual similarity [36]; thus nearest neighbors in  $\mathbf{H}$  define perceptually coherent local neighborhoods.  $\mathbf{G}^k$  promotes local smoothness of the embedding with respect to this current geometry.

2) *OT-based clustering guidance*: Following ExGRG [19], we adapt optimal-transport (OT) clustering guidance to IQA. Let  $\mathbf{C} \in \mathbb{R}^{K \times d_h}$  be  $K$  trainable prototypes and  $\mathbf{A} \in \mathbb{R}^{N \times K}$  the soft *assignments*

$$\mathbf{A}_{j,k} = \frac{\exp(\mathbf{H}_{j,\cdot}^\top \mathbf{C}_{k,\cdot} / \tau_c)}{\sum_{k'} \exp(\mathbf{H}_{j,\cdot}^\top \mathbf{C}_{k',\cdot} / \tau_c)}. \quad (13)$$

Balanced *targets*  $\mathbf{T} \in \mathbb{R}^{N \times K}$  are obtained by a Sinkhorn-Knopp solver with entropy regularization [37], which enforces approximately uniform cluster marginals per mini-batch [38], [39]. For probability vectors  $\mathbf{t}, \mathbf{a} \in [0, 1]^K$  with  $\sum_{k=1}^K t_k = \sum_{k=1}^K a_k = 1$ , we define the cross-entropy

$$\text{CE}(\mathbf{t}, \mathbf{a}) := - \sum_{k=1}^K t_k \log a_k.$$

For notational convenience, we write  $\mathbf{T}_{x_{i,j,k,l}}$  and  $\mathbf{A}_{x_{i,j,k,l}}$  for the rows of  $\mathbf{T}$  and  $\mathbf{A}$  associated with distorted image  $x_{i,j,k,l}$  in Eq. 3. The OT loss has two contributions,

$$\mathcal{L}_{\text{ot}} = \frac{1}{N} \sum_{n=1}^N \text{CE}(\mathbf{T}_{n,\cdot}, \mathbf{A}_{n,\cdot}) + \frac{1}{|\mathcal{P}|} \sum_{(u,v) \in \mathcal{P}} \text{CE}(\mathbf{T}_{u,\cdot}, \mathbf{A}_{v,\cdot}), \quad (14)$$

$$\mathcal{P} = \{(x_{i,j,k,l}, x_{i,j',k,l}) : i \in [B], k \in [C], l \in [L], j \neq j'\}.$$

where  $N$  is the mini-batch size in Eq. 1. The first term aligns each sample's assignment to its own balanced target over all  $N$  images in the mini-batch. The set  $\mathcal{P}$  contains cross-content distorted-image pairs that share the same tiny-batch  $i$ , composition group  $k$ , and severity level  $l$ . The second term averages the corresponding cross-entropy over these pairs.

Soft assignments  $\mathbf{A}$  provide graded membership probabilities, which reduce premature hard assignments and allow clusters to form more flexibly. From  $\mathbf{A}$  we compute an assignment-affinity matrix

$$\mathbf{S}_{i,j}^A = \sum_k \mathbf{A}_{i,k} \log \mathbf{A}_{j,k},$$

then normalize entries and apply a global sparsity limit to obtain the relation graph

$$\mathbf{G}^o = F_{K_g}(\text{norm}(\mathbf{S}^A)) \in \mathbb{R}^{N \times N}, \quad (15)$$

where  $\text{norm}$  maps the matrix entries into  $[0, 1]$  via global min-max normalization, and  $F_{K_g}$  keeps the globally largest  $K_g$  entries, zeroing the rest.

*Intuition.* OT-based guidance shapes the global topology by encouraging samples with similar prototype memberships to remain close across contents, while soft assignments preserve uncertainty during cluster formation. Prototypes  $\mathbf{C}$  and the encoder  $f_\theta$  (hence  $\mathbf{H}$ ) are updated by gradients of  $\mathcal{L}_{\text{ot}}$  together with the overall objective each iteration;  $\mathbf{A}$  and  $\mathbf{T}$  are recomputed from the current features.

#### F. Multi-Source Aggregation with Stop-Gradient

Let

$$\mathbf{S}_G = \{\mathbf{G}^{rd}, \mathbf{G}^{dd}, \mathbf{G}^{rr}, \mathbf{G}^k, \mathbf{G}^o\}.$$

We apply a stop-gradient to each source and combine them with learned nonnegative coefficients:

$$\tilde{\mathbf{G}}^{(i)} = \text{sg}(\mathbf{G}^{(i)}), \quad (16)$$

$$\mathbf{G} = \sum_{\mathbf{G}^{(i)} \in \mathbf{S}_G} \omega_i \tilde{\mathbf{G}}^{(i)}, \quad \omega_i \geq 0, \quad \sum_i \omega_i = 1, \quad (17)$$

where  $\text{sg}(\cdot)$  is the stop-gradient operator (identity in forward, zero gradient in backward). The weights  $\omega$  are produced by a lightweight *hypernetwork*  $\Phi$  [19], [40] from simple per-graph statistics,

$$\omega = \text{softmax}\left(\Phi\left(\{\zeta^{(i)}\}_{i=1}^T\right)\right), \quad (18)$$

$$\zeta^{(i)} = (\text{sum}(\mathbf{G}^{(i)}), \text{nnz}(\mathbf{G}^{(i)})),$$

where  $T = |\mathbf{S}_G|$ ,  $\{\zeta^{(i)}\}_{i=1}^T$  denotes stacking the per-graph statistics over sources,  $\text{sum}(\cdot)$  is the total edge weight (connection mass), and  $\text{nnz}(\cdot)$  is the number of nonzero entries (sparsity). This hypernetwork aggregates an arbitrary set of sources online, adapting  $\omega$  as the graphs evolve during training. The two statistics are inexpensive, scale-agnostic proxies for *strength* and *coverage* of each source, providing a practical signal for allocating weight without hand-tuning.

#### G. Training Details

We maintain sparse relation graphs via the pruning operators  $F_{k_n}$  (Top- $k$  per row) and  $F_{K_d}, F_{K_g}$  (global Top- $K$ ). The graph-weighted invariance  $\mathcal{L}'_{\text{inv}}$  is then evaluated as  $\sum_{(i,j): \mathbf{G}_{ij} > 0} \mathbf{G}_{ij} \|\mathbf{Z}_{i,\cdot} - \mathbf{Z}_{j,\cdot}\|_2^2$ , i.e., only over nonzero edges rather than all  $N^2$  pairs; this respects sparsification and reduces computation. We include the graph regularizer

$$\mathcal{R}_{\text{graph}} = - \sum_{i,j} \mathbf{G}_{i,j}^2,$$

to encourage nontrivial mass on the retained edges after sparsification. Under the simplex constraint on  $\omega$ , this favors informative retained edge weights instead of vanishing graph mass. Our construction choices keep all graph entries in  $[0, 1]$ , which avoids uncontrolled saturation.

#### H. End-to-End Optimization and Regression Protocol

The full objective is

$$\mathcal{L}_{\text{total}} = \mathcal{L}_{\text{ssl}} + \eta \mathcal{L}_{\text{ot}} + \xi \mathcal{R}_{\text{graph}}. \quad (19)$$

In each iteration, we construct  $\mathbf{G}$  from the current representations, then update the encoder  $f_\theta$ , projector  $g_\psi$ , the prototype parameters, and the aggregation hypernetwork  $\Phi$  by minimizing Eq. 19 while applying stop-gradient through  $\mathbf{G}$ . After pre-training,  $g_\psi$  is discarded and  $f_\theta$  is frozen; we then train a linear regressor on the encoder features  $\mathbf{H}$  to predict human opinion scores.

## IV. EXPERIMENTAL EVALUATION

We evaluate SHAMISA on standard NR-IQA benchmarks with a linear-probe protocol [11], [17], [18], report SRCC and PLCC, and study within-dataset performance, cross-dataset transfer, gMAD diagnostics, representation visualizations, ablations, and a full-reference extension.

### A. Setup

*a) Backbone and pretext:* We initialize a ResNet-50 encoder  $f_\theta$  from ImageNet and *pre-train* it self-supervised with  $\mathcal{L}_{\text{total}}$  (Eq. 19), which couples VICReg-style variance/covariance terms with a graph-weighted invariance term. A 2-layer MLP projector  $g_\psi$  is used only during pre-training. Unlabeled inputs are degraded online by the compositional distortion engine (Sec. III). Unless otherwise noted, training uses sparse relation graphs  $\mathbf{G}^{rd}$ ,  $\mathbf{G}^{dd}$ ,  $\mathbf{G}^{rr}$ ,  $\mathbf{G}^k$ ,  $\mathbf{G}^o$  aggregated by  $\Phi$ . After pre-training,  $g_\psi$  is discarded and  $f_\theta$  is frozen for all evaluations.

*b) Training details:* We pre-train for one epoch over the 140k KADIS reference images with SGD. Encoder and projector dimensions are  $d_n=2048$  and  $d_z=256$ . Each update uses  $B=2$  tiny-batches,  $R=3$  references,  $C=4$  composition groups, and  $L=5$  severity levels, giving  $N_{\text{ref}}=BR=6$ ,  $N_{\text{comp}}=CL=20$ , and  $N=N_{\text{ref}}(N_{\text{comp}}+1)=126$  in Eq. 1. Distortion generation uses  $M_d=7$ . Graph sparsity and OT settings are  $k_n=31$ ,  $K_d=4096$ ,  $K=32$ , and  $\tau_c=0.1$ ; for the OT graph, the effective global sparsification budget scales with mini-batch size through  $K_g=8N$ . Crop size is  $224 \times 224$ . Remaining details are listed in §A.

### B. Datasets and Evaluation Protocol

*a) Pre-training data:* Following ARNIQA [18], we use the 140k pristine images from KADIS [9] as content sources to enable a fair comparison under a shared pre-training corpus. We generate degradations online with our compositional distortion engine.

*b) Evaluation datasets:* We include both synthetic and in-the-wild benchmarks. Synthetic: LIVE [41], CSIQ [42], TID2013 [43], KADID-10K [9]. In-the-wild: FLIVE [29], SPAQ [44]. Brief dataset statistics are available in Appendix D.

*c) Protocol:* We follow SSL-IQA practice [11], [17], [18]. For LIVE, CSIQ, TID2013, KADID-10K, and SPAQ, we create 10 train/val/test splits, using reference-disjoint sampling on the synthetic datasets and random 70/10/20 splits on SPAQ. For FLIVE, we use the official split [29]. We train an  $\ell_2$  ridge regressor [45] on frozen features and select  $\alpha_{\text{ridge}}$  from a log-spaced grid of 100 values in  $[10^{-3}, 10^3]$  by maximizing median validation SRCC across the available splits. At test time, we extract features at full and half scale and concatenate [17], then average predictions over five deterministic crops per image (four corners and center) [10]. We report the median over the repeated splits where applicable. PLCC is computed after the standard four-parameter logistic mapping [46].

### C. Compared Methods

We compare against traditional NR-IQA (BRISQUE [20], NIQE [21]), codebook models (CORNIA [24], HOSA [25]), and deep supervised NR-IQA (DB-CNN [6], HyperIQA [7], TRes [8], Su et al. [47]). We also include SSL-IQA baselines CONTRIQUE [17], Re-IQA [11], and ARNIQA [18], matching the methods reported in Table I.

### D. Within-Dataset Performance

Table I shows that SHAMISA attains the best SRCC and PLCC on LIVE, CSIQ, and TID2013, while remaining competitive on KADID-10K, FLIVE, and SPAQ under the frozen-encoder linear-probe protocol. On KADID-10K, SHAMISA ranks behind CONTRIQUE but ahead of ARNIQA, which is consistent with KADID-10K closely matching the synthetic distortion families emphasized by CONTRIQUE’s pre-training scheme. For authentic images, SHAMISA is second on FLIVE and remains competitive on SPAQ, trailing Re-IQA by a narrow margin. This suggests a stronger balance between synthetic and authentic performance than methods that are markedly stronger on only one side. Overall, SHAMISA achieves the strongest six-dataset average SRCC and PLCC among the SSL methods reported here, with average SRCC/PLCC of 0.886/0.904.

We attribute these gains to two factors: a compositional distortion engine that forms single-factor severity trajectories, and dual-source relation graphs that fuse metadata-driven and structure-intrinsic relations within a graph-weighted VICReg objective. These gains do not come from a materially larger training budget. Under the same KADIS (140k) protocol on an NVIDIA H100 80GB (HBM3), end-to-end pre-training plus evaluation on the six NR-IQA benchmarks takes approximately 12.5 hours for ARNIQA and 13.5 hours for SHAMISA. Re-IQA is more training-intensive, as it additionally trains a content encoder on ImageNet and a separate quality encoder with large augmentation schedules.

### E. Cross-Dataset Transfer

*a) Cross-dataset transfer:* Table II shows that SHAMISA attains the best SRCC on 9 of the 12 synthetic transfer directions, ranks second on 2 more, and remains competitive on the remaining case. Relative to ARNIQA, the clearest gains appear when the source dataset covers fewer distortion types, such as LIVE or CSIQ, and the target is more diverse, such as TID2013 or KADID-10K. This pattern is visible in LIVE  $\rightarrow$  CSIQ, LIVE  $\rightarrow$  TID2013, CSIQ  $\rightarrow$  TID2013, and TID2013  $\rightarrow$  KADID-10K, suggesting that the learned representation aligns distortion structure across contents in a way a linear regressor can exploit. The main exception is LIVE  $\rightarrow$  KADID-10K, where ARNIQA and CONTRIQUE retain an advantage. KADID-10K  $\rightarrow$  LIVE is another difficult direction, where HyperIQA remains strongest and SHAMISA ranks second. This pattern is consistent with LIVE being smaller and perceptually milder, leaving less headroom for severity-aware supervision.

*b) Protocol:* We follow the standard SSL-IQA linear-probe setting: the encoder is frozen; we train a ridge regressor on the train split of the source dataset, select its regularization on the source val split, and evaluate zero-shot on the target test split with identical multi-scale features and five-crop pooling. We report the median over 10 reference-disjoint splits. This transfer style mirrors practical deployment. A large pool of unlabeled images is used for SSL pre-training, and only a small labeled set from a related source dataset is available to fit a lightweight head. The model must then generalize to a

TABLE I

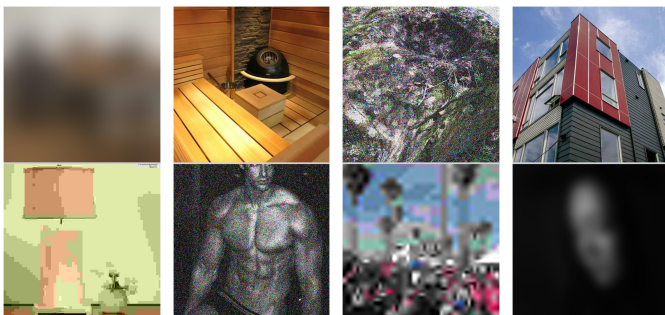
PERFORMANCE COMPARISON ON SYNTHETIC AND IN-THE-WILD NR-IQA DATASETS. WE REPORT SRCC AND PLCC. BEST AND SECOND-BEST PER COLUMN ARE **BOLD** AND UNDERLINED. PRIOR NUMBERS ARE TAKEN FROM THEIR PAPERS OR PUBLIC CODE WHERE AVAILABLE [11], [17], [18].

Method	Type	Synthetic distortions								Authentic distortions					
		LIVE		CSIQ		TID2013		KADID-10K		FLIVE		SPAQ		Average	
		SRCC	PLCC	SRCC	PLCC	SRCC	PLCC	SRCC	PLCC	SRCC	PLCC	SRCC	PLCC	SRCC	PLCC
BRISQUE [20]	Handcrafted	0.939	0.935	0.746	0.829	0.604	0.694	0.528	0.567	0.288	0.373	0.809	0.817	0.652	0.703
NIQE [21]	Handcrafted	0.907	0.901	0.627	0.712	0.315	0.393	0.374	0.428	0.211	0.288	0.700	0.709	0.522	0.572
CORNIA [24]	Codebook	0.947	0.950	0.678	0.776	0.678	0.768	0.516	0.558	–	–	0.709	0.725	–	–
HOSA [25]	Codebook	0.946	0.950	0.741	0.823	0.735	0.815	0.618	0.653	–	–	0.846	0.852	–	–
DB-CNN [6]	Supervised	0.968	0.971	0.946	0.959	0.816	0.865	0.851	0.856	0.554	0.652	0.911	0.915	0.841	0.870
HyperIQA [7]	Supervised	0.962	0.966	0.923	0.942	0.840	0.858	0.852	0.845	0.535	0.623	<u>0.916</u>	0.919	0.838	0.859
TReS [8]	Supervised	0.969	0.968	0.922	0.942	0.863	0.883	0.859	0.858	0.554	0.625	–	–	–	–
Su et al. [47]	Supervised	<u>0.973</u>	<u>0.974</u>	0.935	0.952	0.815	0.859	0.866	0.874	–	–	–	–	–	–
CONTRIQUE [17]	SSL+LR	0.960	0.961	0.942	0.955	0.843	0.857	<b>0.934</b>	<b>0.937</b>	0.580	0.641	0.914	0.919	0.862	0.878
Re-IQA [11]	SSL+LR	0.970	0.971	0.947	0.960	0.804	0.861	0.872	0.885	<b>0.645</b>	<b>0.733</b>	<b>0.918</b>	<b>0.925</b>	0.859	0.889
ARNIQA [18]	SSL+LR	0.966	0.970	<u>0.962</u>	<u>0.973</u>	<u>0.880</u>	<u>0.901</u>	<u>0.908</u>	<u>0.912</u>	0.595	0.671	0.905	0.910	<u>0.869</u>	<u>0.890</u>
<b>SHAMISA (ours)</b>	SSL+LR	<b>0.986</b>	<b>0.987</b>	<b>0.981</b>	<b>0.987</b>	<b>0.904</b>	<b>0.919</b>	0.922	0.924	<u>0.610</u>	<u>0.688</u>	0.914	<u>0.920</u>	<b>0.886</b>	<b>0.904</b>

TABLE II

CROSS-DATASET SRCC ON SYNTHETIC NR-IQA BENCHMARKS. BEST AND SECOND-BEST PER ROW ARE **BOLD** AND UNDERLINED. BASELINE VALUES ARE TAKEN FROM PRIOR REPORTS IN ARNIQA AND RE-IQA [11], [18].

Training	Testing	HyperIQA	Su et al.	CONTRIQUE	Re-IQA	ARNIQA	SHAMISA
LIVE	CSIQ	0.744	0.777	0.803	0.795	<u>0.904</u>	<b>0.909</b>
LIVE	TID2013	0.541	0.561	0.640	0.588	<u>0.697</u>	<b>0.700</b>
LIVE	KADID-10K	0.492	0.506	<u>0.699</u>	0.557	<b>0.764</b>	0.694
CSIQ	LIVE	0.926	<u>0.930</u>	0.912	0.919	0.921	<b>0.939</b>
CSIQ	TID2013	0.541	0.550	0.570	0.575	<u>0.721</u>	<b>0.729</b>
CSIQ	KADID-10K	0.509	0.515	0.696	0.521	<b>0.735</b>	<u>0.711</u>
TID2013	LIVE	0.876	0.892	<u>0.904</u>	0.900	0.869	<b>0.908</b>
TID2013	CSIQ	0.709	0.754	0.811	0.850	<u>0.866</u>	<b>0.870</b>
TID2013	KADID-10K	0.581	0.554	0.640	0.636	<u>0.726</u>	<b>0.779</b>
KADID-10K	LIVE	<b>0.908</b>	0.896	0.900	0.892	0.898	0.901
KADID-10K	CSIQ	0.809	0.828	0.773	0.855	<u>0.882</u>	<b>0.892</b>
KADID-10K	TID2013	0.706	0.687	0.612	0.777	0.760	<b>0.779</b>



(a) SHAMISA, low bin (b) SHAMISA, high bin (c) ARNIQA, low bin (d) ARNIQA, high bin

Fig. 2. gMAD on Waterloo Exploration (distorted pool): panels (a,b) use SHAMISA as the defender and panels (c,d) use ARNIQA as the defender. In each panel, the top and bottom images are the attacker-selected pair from the indicated defender-quality bin, with low-bin cases shown in (a,c) and high-bin cases shown in (b,d). Appendix Table VII reports the corresponding top-1 attacker gaps.

related but distinct target without target labels and without adapting normalization statistics to the target dataset. Full details are provided in Appendix F.

### F. gMAD Diagnostic on Waterloo

We use the group maximum differentiation (gMAD) protocol [48] as a pairwise diagnostic on the Waterloo Exploration Database [49] using its distorted image pool (no MOS annotations). Following our standard NR-IQA evaluation pipeline, we convert frozen representations into scalar quality

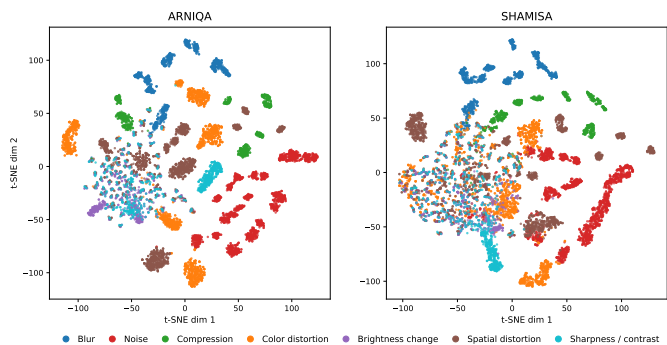


Fig. 3. t-SNE visualization of image-level encoder representations on KADID-10K. We extract encoder representations  $\mathbf{H}$  (pre-projector) and average across crops to obtain one representation per image, yielding 10,125 image-level points. Points are colored by the coarse distortion family using a shared fixed palette. Compared to ARNIQA, SHAMISA exhibits clearer coarse-family structure for several dominant degradation families, while both models show overlap among visually related families such as brightness and color manipulations. This visualization is a qualitative diagnostic and does not affect the quantitative evaluation protocol.

predictions by fitting a ridge regressor on KADID-10K and then apply the resulting predictors to all Waterloo images. Given a defender model, we first split the pool into equal-count bins based on the defender’s predicted quality. Within a chosen bin, the attacker then selects the image pair with the largest attacker-side score gap while the defender still scores the pair similarly. Appendix I gives the corresponding protocol details. Fig. 2 shows representative pairs for low and high defender levels in both defender-attacker directions, and Appendix Table VII reports the corresponding top-1 attacker gaps. In this pairwise Waterloo gMAD comparison with KADID-trained ridge heads, attacker gaps are smaller when SHAMISA is the defender than when ARNIQA is the defender, suggesting tighter within-bin quality consistency for SHAMISA in this specific setting.

### G. t-SNE Representation Visualization

We visualize the structure of the learned representation space by applying 2D t-SNE [50] to image-level encoder representations  $\mathbf{H}$  on KADID-10K [9]. For each image, we extract  $\mathbf{H}$  (pre-projector) and average across crops, yielding

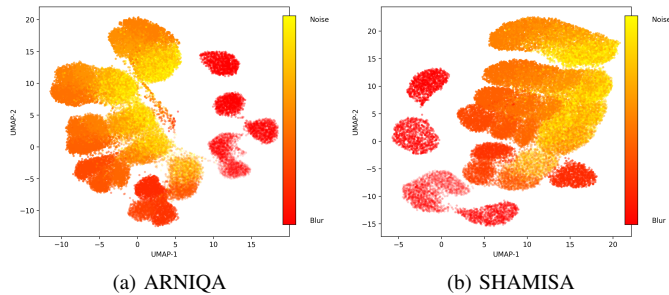


Fig. 4. **Manifold visualization with UMAP [51]** using encoder representations  $\mathbf{H}$  extracted from 1,000 pristine KADIS images degraded with Gaussian blur and white noise. For each pristine image we generate 5 blur-only samples, 5 noise-only samples, and all  $5 \times 5$  blur $\rightarrow$ noise compositions (35 variants per image, 35k total points). Point color is the weighted average of blur (red) and noise (yellow) according to their relative intensities; marker opacity increases with total severity.

10,125 points. Fig. 3 colors points by coarse distortion family using a shared, fixed palette for fair visual comparison. Both methods separate several major degradation families, but SHAMISA often forms more coherent regions for prominent categories, whereas ARNIQA shows more inter-family mixing in the central area. We provide additional severity-colored visualizations and subtype-level views (by distortion family) in Appendix G. Across these plots, separability is strongest for families with distinctive artifact statistics (e.g., blur, noise, and compression), while brightness-related manipulations remain more entangled and challenging for both models. Overall, these plots are consistent with SHAMISA’s pre-training encouraging a representation geometry that is coherent across major distortion families while still preserving fine-grained variation within them.

#### H. UMAP Manifold Visualization

We visualize the distortion manifold induced by two degradations and their compositions using UMAP [51]. We sample 1,000 pristine images from KADIS and generate 35 degraded variants per image: 5 blur-only samples, 5 noise-only samples, and all  $5 \times 5$  blur $\rightarrow$ noise compositions, where blur is applied before noise. We then extract pooled encoder features  $\mathbf{H}$  (pre-projector) with frozen weights and embed them into 2D using identical UMAP hyperparameters across models (Fig. 4). Protocol details are given in Appendix H. UMAP is fit independently for each model, so the absolute axes are not aligned across panels. We therefore compare the internal organization of each panel, rather than point-by-point coordinates across panels.

Across both models, compositions tend to lie closer to the noise region, consistent with noise being applied after blur and thus remaining visually dominant in the final image. However, the geometry differs markedly between ARNIQA and SHAMISA. The ARNIQA embedding contains a large, diffuse interior region where samples with different blur-to-noise mixtures overlap strongly, yielding a weak and locally inconsistent color gradient. In contrast, SHAMISA appears to produce a more organized manifold, with clearer bands and a smoother progression from blur-dominated (red) to noise-dominated (yellow) compositions, as well as fewer ambigu-

TABLE III  
MAIN ABLATIONS. MEDIAN OVER 10 SPLITS PER DATASET; THEN AVERAGED.  $\text{SRCC}_s/\text{PLCC}_s$  AVERAGE OVER SYNTHETIC  $\{\text{LIVE}, \text{CSIQ}, \text{TID2013}, \text{KADID-10K}\}$ ,  $\text{SRCC}_a/\text{PLCC}_a$  OVER AUTHENTIC  $\{\text{FLIVE}, \text{SPAQ}\}$ , AND  $\text{SRCC}_g/\text{PLCC}_g$  DENOTE THE AVERAGE OVER THE SIX PER-DATASET MEDIAN  $\text{SRCC}/\text{PLCC}$  VALUES. FULL ABLATION CATALOG IS REPORTED IN APPENDIX TABLE VIII.

Variant	$\text{SRCC}_g$	$\text{PLCC}_g$	$\text{SRCC}_a$	$\text{PLCC}_a$	$\text{SRCC}_s$	$\text{PLCC}_s$
<b>A0: SHAMISA</b>	0.8862	0.9042	0.7620	0.8040	0.9483	0.9543
<i>(A) Aggregation &amp; regularization</i>						
A1: Binary $\mathbf{G}$	0.8767	0.8924	0.7475	0.7821	0.9374	0.9457
A3: No $\Phi$ (fixed linear mixture)	0.8759	0.8951	0.7479	0.7896	0.9361	0.9457
<i>(B) Graph sources</i>						
B1: No $\mathbf{G}^o$ (OT graph)	0.8600	0.8787	0.7661	0.8069	0.8995	0.9092
B7: Metadata only $\{\mathbf{G}^{rd}, \mathbf{G}^{dd}, \mathbf{G}^{rr}\}$	0.8467	0.8648	0.7634	0.8010	0.8801	0.8905
B6: $\mathbf{G}^k$ only	0.7891	0.8018	0.7577	0.7825	0.7922	0.8017
B8: Structure only $\{\mathbf{G}^k, \mathbf{G}^o\}$	0.8753	0.8961	0.7419	0.7891	0.9387	0.9475
<i>(D) Distortion engine</i>						
D1: $M_d=1$	0.8775	0.9077	0.7259	0.7684	0.9519	0.9783
D2: Discrete severities ( $L=5$ )	0.8767	0.8987	0.7456	0.7890	0.9386	0.9518
D4: Fixed order $\pi$	0.8587	0.8712	0.7434	0.7668	0.9113	0.9215
<i>(E) Objective diagnostic</i>						
E1: No $\mathcal{L}_{ot}$	0.7887	0.8009	0.7597	0.7836	0.7904	0.7996

ous mixed-mixture points concentrated in the middle. This qualitative diagnostic suggests that SHAMISA more explicitly parameterizes the two distortion axes under composition: blur and noise vary more smoothly, and with less central mixing than ARNIQA.

#### I. Ablations

*a) Ablation design:* We ablate SHAMISA along complementary axes that map directly to our main design choices: (A) *how* we aggregate multi-source relations into the soft matrix  $\mathbf{G}$  (learned end-to-end mixing  $\Phi$  vs fixed mixing; regularization), (B) *which* relation sources are necessary (structure graphs  $\mathbf{G}^k, \mathbf{G}^o$  vs metadata graphs  $\mathbf{G}^{rd}, \mathbf{G}^{dd}, \mathbf{G}^{rr}$ ), (C) *how* we sparsify the global OT graph (global vs row-wise truncation), (D) *how* the compositional distortion engine defines the self-supervised training distribution (composition complexity, severity modeling, ordering), and (E–F) objective diagnostics that isolate the contribution of OT alignment and severity-dependent edge weighting. Each variant changes only minimal factors relative to the reference configuration (A0). We evaluate on six NR-IQA datasets (LIVE, CSIQ, TID2013, KADID-10K, FLIVE, SPAQ) with 10 random splits per dataset, reporting the median test  $\text{SRCC}/\text{PLCC}$  per dataset, then summarizing synthetic and authentic groups separately together with a global comparison score. For readability, Table III highlights the most diagnostic variants; the complete catalog is deferred to Appendix Table VIII.

*b) Results and analysis:* A0 achieves  $\text{SRCC}_g=0.8862$  ( $\text{PLCC}_g=0.9042$ ), with  $\text{SRCC}_s=0.9483$  and  $\text{SRCC}_a=0.7620$ . Across all variants (Appendix Table VIII), three consistent trends emerge that directly support SHAMISA’s key claims. First, *global OT structure is the dominant structural prior*: removing the OT alignment term (E1) yields the largest degradation ( $\text{SRCC}_g=0.7887$ ), and removing the OT-derived global graph  $\mathbf{G}^o$  (B1) causes the strongest drop among single-source removals (0.8600). Together, these results indicate that SHAMISA’s gains are not explained by generic instance-level invariances alone; rather, OT-guided relations enforce long-range consistency that shapes the global geometry of the

learned quality manifold and is difficult to recover from local neighborhoods.

Second, *multi-source relational supervision is necessary, with structure and metadata playing complementary roles*. The single-family variants are substantially worse than A0: using only local structure  $\mathcal{G}^k$  (B6) collapses to  $\text{SRCC}_g=0.7891$ , while metadata-only graphs (B7) improve to 0.8467 but remain far from A0. This separation clarifies the contribution of each novelty: structural graphs preserve local neighborhoods that emerge in the evolving representation space, thereby stabilizing a content-consistent geometry rather than forcing similarity from distortion metadata alone, while metadata graphs inject distortion semantics that are not reliably inferable from pixels alone, especially under authentic mixtures. Consistent with this view, structure-only  $\{\mathcal{G}^k, \mathcal{G}^o\}$  (B8) is competitive on synthetic data ( $\text{SRCC}_s=0.9387$ ) but drops on authentic data ( $\text{SRCC}_a=0.7419$ ), highlighting that metadata relations mainly contribute robustness to real-world content and capture-device shifts. In contrast, removing any single metadata edge type (B3–B5) produces only modest changes, suggesting each metadata relation is individually weak but collectively beneficial.

Third, *the distortion engine benefits from both composition diversity and realistic severity modeling*. Restricting compositions to a single atomic distortion (D1,  $M_d=1$ ) still yields very strong synthetic performance ( $\text{SRCC}_s=0.9519$ ), but it reduces authentic performance ( $\text{SRCC}_a$ : 0.7259 vs 0.7620) and slightly lowers global SRCC relative to A0. This suggests that richer compositions matter for the mixed degradations encountered beyond synthetic benchmarks. Moreover, fixing the composition order (D4) substantially harms performance ( $\text{SRCC}_g=0.8587$ ), directly supporting the need for stochastic composition diversity to prevent overfitting to a narrow degradation trajectory. Severity modeling also matters: discretizing severities (D2,  $L=5$ ) reduces  $\text{SRCC}_g$  to 0.8767, suggesting that coarse severity quantization weakens the smooth relative-order information that the metadata graphs can exploit. Using uniform severity sampling (D3) also degrades performance slightly (0.8743), consistent with the default severity sampling favoring milder distortions and avoiding an overrepresentation of unrealistic extreme cases.

Finally, ablations of relation aggregation indicate that *how* relations are mixed matters, but the effects are necessarily smaller than removing relations entirely. Binarizing  $\mathcal{G}$  (A1) slightly reduces  $\text{SRCC}_g$  (0.8767), supporting soft relation strengths for graded supervision. Replacing learned mixing  $\Phi$  with fixed linear mixing (A3) decreases  $\text{SRCC}_g$  to 0.8759, consistent with  $\Phi$  learning to reweight heterogeneous relation sources. Removing the graph regularizer  $\mathcal{R}_{\text{graph}}$  (A2) yields only a small drop in  $\text{SRCC}_g$  (0.8813), suggesting that it mainly improves stability and calibration rather than acting as a dominant source of the gains.

### J. Pre-training Dynamics

We track downstream NR-IQA performance during SSL pre-training by periodically freezing the encoder and fitting a lightweight regressor on each target dataset. Frozen checkpoints are evaluated every 5000 training steps. Fig. 5 shows

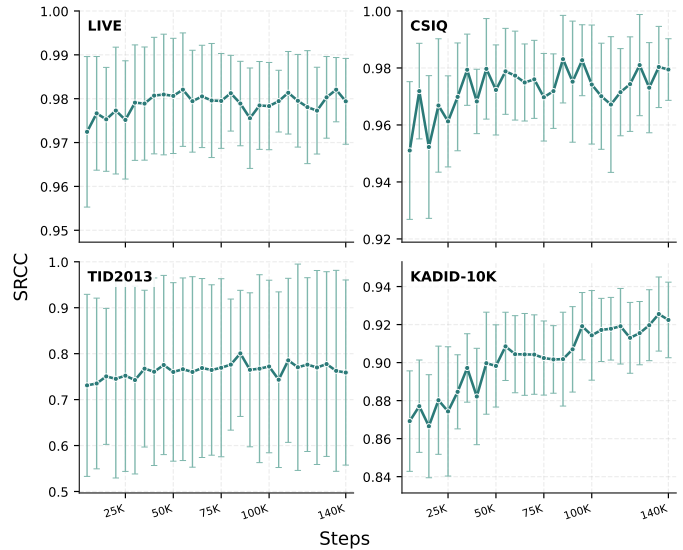


Fig. 5. **SRCC vs. training steps during SSL pre-training** (mean with  $\pm$  std error bars over 10 splits) across representative NR-IQA benchmarks. Curves typically rise early and then saturate, while the best checkpoint can vary by dataset since the SSL objective is not identical to downstream SRCC.

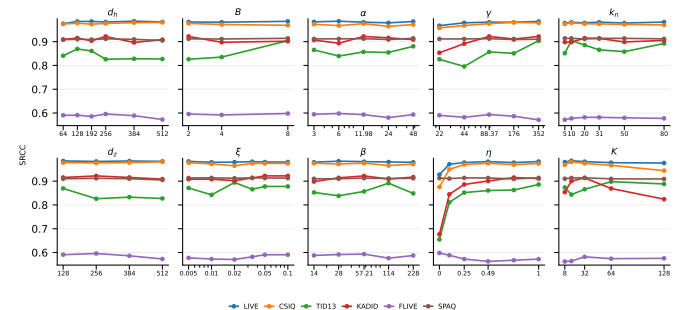


Fig. 6. **One-at-a-time sweeps around the SHAMISA reference A0**, reporting SRCC across six NR-IQA benchmarks in a single merged view. Columns correspond to  $(d_h, d_z)$ ,  $(B, \xi)$ ,  $(\alpha, \beta)$ ,  $(\gamma, \eta)$ , and  $(k_n, K)$ , with a shared legend across all panels.

that SRCC improves rapidly in the early phase and then saturates across the representative benchmark datasets shown here, indicating that the learned representation becomes useful for quality prediction relatively early in pre-training.

Importantly, the best checkpoint can be dataset-dependent: while some datasets continue to improve or remain stable as pre-training proceeds, others exhibit a mild peak-and-decline behavior, which is expected because the SSL objective is not optimized directly for SRCC on any single benchmark. As a deployment note, when a small labeled validation set is available in the target domain, it can be used to select a checkpoint for that domain. Unless stated otherwise, all results reported in Tables I and II use the fixed A0 checkpoint; this section is a diagnostic and is not used for model selection. Additional diagnostic figures are provided in Appendix K.

### K. Hyperparameter Sensitivity

We analyze hyperparameter sensitivity by varying one knob at a time around our A0 configuration while keeping the rest fixed. Fig. 6 shows that most capacity and graph-construction

choices admit broad plateaus:  $d_h$ ,  $d_z$ , and  $k_n$  typically yield stable SRCC across a wide range, and increasing  $K$  mainly saturates after moderate values. In contrast, the OT alignment coefficient  $\eta$  is the most influential knob across datasets, with the largest SRCC swings on synthetic distortion benchmarks such as TID2013 and KADID-10K, suggesting that overly weak alignment under-utilizes relational guidance, whereas overly strong alignment can over-constrain representations. Among VICReg terms, the invariance weight  $\gamma$  exhibits the clearest sensitivity, particularly on FLIVE, whereas the variance and covariance weights  $\alpha$  and  $\beta$  are comparatively robust across the tested ranges. Overall, these sweeps indicate that SHAMISA is robust across broad ranges of capacity and graph-design choices, while a smaller set of alignment-related coefficients, especially  $\eta$  and  $\gamma$ , remains important for fine control. Appendix L reports the corresponding SRCC sensitivity summary.

*a) FR extension:* We also propose a full-reference variant, SHAMISA-FR, that reuses the frozen no-reference encoder and uses the absolute feature difference  $|h_{\text{ref}} - h_{\text{dist}}|$  between pristine and distorted images as the regressor input. This variant requires no additional backbone pre-training and attains competitive FR-IQA accuracy; details are provided in Appendix E, with the main comparison in Appendix Table VI.

*b) Reproducibility:* Additional implementation details, optimization settings, evaluation protocols, and supplementary diagnostics are provided in Appendices A, F, K, and L. The project repository is available at <https://github.com/Mahdi-Naseri/SHAMISA/>.

## V. CONCLUSION

We presented **SHAMISA**, a non-contrastive self-supervised framework for NR-IQA that learns unified distortion-aware and content-aware representations. SHAMISA couples a compositional distortion engine with single-factor variation to generate controllable severity trajectories, and supervises learning through dual-source relation graphs that fuse Metadata-Driven Graphs with Structurally Intrinsic Graphs. These relations drive a graph-weighted VICReg-style invariance with clustering-guided supervision. In each iteration, we construct the graphs from the current representations and then update the model with stop-gradient. This yields a frozen encoder whose features support accurate quality prediction with a linear regressor. Across synthetic and authentic benchmarks, SHAMISA achieves the strongest overall average among the SSL methods compared here, with improved cross-dataset generalization and stronger gMAD diagnostics, while using no human quality labels during pre-training. A full-reference variant, SHAMISA-FR, reuses the same frozen encoder without additional backbone training and attains competitive FR-IQA accuracy. Future work includes exploiting the learned topology for blind image restoration and extending the framework to video quality assessment.

## Supplementary Material for “SHAMISA: SHAped Modeling of Implicit Structural Associations for Self-supervised No-Reference Image Quality Assessment”

Mahdi Naseri and Zhou Wang

### APPENDIX A ARCHITECTURES AND OPTIMIZATION

Table IV summarizes the fixed SHAMISA pre-training configuration used across all experiments; unless stated otherwise, downstream evaluation selects the ridge regularization  $\alpha_{\text{ridge}}$  per dataset on the validation split, as described in Sec. IV-B.

Implementation detail for graph construction: diagonal self-edges are removed from all source graphs before aggregation. We therefore do not use self-invariance edges in Eq. 7.

### APPENDIX B COMPOSITIONAL DISTORTION ENGINE

We use the compositional engine of Sec. III-B with  $M_d = 7$  and per-update structure  $B = 2$  tiny-batches, each with  $R = 3$  pristine references and  $C = 4$  distortion composition groups. Each group forms a single-factor trajectory with  $L = 5$  levels, generating images  $x_{i,j,k,l}$  as defined in Eq. 3. Normalized severities are sampled i.i.d. by drawing  $\epsilon \sim \mathcal{N}(0, 0.5^2)$  and setting  $s = \min(1, |\epsilon|)$ ; within each group, one distortion coordinate varies across  $L$  i.i.d. draws  $\{s^{(l)}\}_{l=1}^L$ , which are kept in sampled order and are not forced to include either endpoint of the severity range, while all other coordinates are held at their baseline sampled values. Distortion functions are applied sequentially in a uniformly random order (Eq. 2).

### APPENDIX C EVALUATION DETAILS

Following prior SSL-IQA evaluation practice [11], [17], [18], we use two scales per image (full and half) and five deterministic crops per scale [10], [17], with ridge regularization selected on the validation split as in Sec. IV-B. We report the median over 10 random splits where applicable. On synthetic datasets, the splits are reference-disjoint following [11], [17], [18]. For FLIVE we use the official split [29], and for SPAQ we use random 70/10/20 splits. PLCC follows the same four-parameter logistic mapping specified in Sec. IV-B.

### APPENDIX D DATASETS

We evaluate on four synthetic IQA benchmarks and two authentic in-the-wild IQA benchmarks. Table V summarizes the dataset sizes, label types, and split notes used throughout the paper.

Among the authentic datasets, FLIVE provides large-scale in-the-wild images with both image-level and patch-level quality annotations [29], whereas SPAQ focuses on smartphone photography captured under diverse real-world conditions [44]. For SPAQ, we resize the shorter side to 512 as in [44].

### APPENDIX E SHAMISA-FR: FULL-REFERENCE VARIANT

a) *Setup*: SHAMISA-FR reuses the pre-trained  $f_\theta$  from the no-reference setting and keeps it frozen. A key point is that the FR variant adds only a lightweight regressor on top of frozen features, so it requires no additional backbone pre-training and only minimal extra computation. Given  $(x_{\text{ref}}, x_{\text{dist}})$ , we compute

$$h_{\text{ref}} = f_\theta(x_{\text{ref}}), \quad h_{\text{dist}} = f_\theta(x_{\text{dist}}),$$

then form  $u = |h_{\text{ref}} - h_{\text{dist}}|$ . A linear regressor is trained on  $u$  to predict the quality label (DMOS for LIVE/CSIQ, MOS for TID2013/KADID-10K) without updating  $f_\theta$ .

b) *Protocol*: We evaluate on four synthetic FR-IQA datasets (LIVE, CSIQ, TID2013, KADID-10K), using the same split logic as in our NR evaluation, and report median SRCC/PLCC over 10 random splits. For context, Table VI also lists representative FR-IQA baselines as reported in prior work [17], [18], [58].

c) *Results*: Table VI shows that SHAMISA-FR is most competitive on CSIQ among the SSL-based FR rows, while remaining competitive on LIVE and trailing more clearly on TID2013 and KADID-10K, which cover a broader mix of distortions. Supervised FR baselines remain stronger because they optimize full networks directly on the target FR datasets, whereas SHAMISA-FR deliberately tests how far a frozen no-reference representation can transfer with only a lightweight head. As the backbone is fixed, these results primarily reflect the pre-trained representation.

### APPENDIX F CROSS-DATASET EVALUATION PROTOCOL

a) *Practical motivation*: The protocol is designed to reflect common deployment constraints in no-reference quality assessment. In practice, one has abundant unlabeled images for self-supervised pre-training, a limited labeled dataset from a related source domain to fit a lightweight head, and a target distribution that is similar but not identical, with little to no supervision. Freezing the encoder, avoiding any target-specific normalization, and disallowing target-time hyperparameter tuning isolate representation quality and prevent leakage across domains.

b) *Setting*: We assess zero-shot transfer across synthetic NR-IQA datasets {LIVE, CSIQ, TID2013, KADID-10K}. The encoder  $f_\theta$  is frozen for all evaluations and pre-trained once under the setup of Sec. IV-A. Only a ridge regressor is trained per source dataset.

c) *Source-target procedure*: For each source dataset  $D_s$ , we create 10 reference-disjoint 70/10/20 train/val/test splits on  $D_s$ . We extract frozen features at two scales and five crops per scale, concatenate features, and train a ridge regressor on the train split of  $D_s$ . The regularization coefficient is selected once on the val split of  $D_s$  via a logarithmic grid from  $10^{-3}$  to  $10^3$ . The selected regressor is then evaluated, without any modification, on the test split of every target  $D_t \neq D_s$ .

TABLE IV

ESSENTIAL FINAL HYPERPARAMETERS USED FOR SHAMISA PRE-TRAINING. A SINGLE CONFIGURATION IS SHARED ACROSS ALL DATASETS (NO DATASET-SPECIFIC TUNING DURING SSL).

Group	Hyperparameters
Architecture	ResNet-50 encoder; $d_h = 2048$ ; projector output $d_z = 256$ .
Optimization	SGD with lr = $1.5 \times 10^{-3}$ , momentum 0.9, weight decay $10^{-4}$ , and cosine annealing warm restarts.
Loss	VICReg-style weights $(\alpha, \beta, \gamma) = (11.98, 57.21, 88.37)$ ; OT alignment weight $\eta = 0.4906$ ; graph regularizer weight $\xi = 0.0342$ .
Graphs	kNN graph: $k_n = 31$ ; metadata graph sparsifier: $K_d = 4096$ ; ref-ref edge weight $w_{rr} = 0.5766$ ; OT graph: $K = 32$ , $\tau_c = 0.1$ ; OT global sparsifier: $K_g = 8N$ .
Distortion engine	Per update: $B = 2$ tiny-batches, $R = 3$ references, $C = 4$ composition groups, $L = 5$ severity levels; crop size 224; max distortions per sample $M_d = 7$ .

TABLE V

DATASET STATISTICS FOR THE NR-IQA BENCHMARKS. SYNTHETIC DATASETS ARE REPORTED BY REFERENCE COUNT AND DISTORTION INVENTORY, WHEREAS AUTHENTIC DATASETS ARE SUMMARIZED BY IMAGE COUNT AND LABEL TYPE.

Dataset	Type	Pristine refs	Distortion types	Images	Label type	Split note
LIVE [41]	Synthetic	29	5	779	DMOS	Reference-disjoint
CSIQ [42]	Synthetic	30	6	866	DMOS	Reference-disjoint
TID2013 [43]	Synthetic	25	24	3000	MOS	Reference-disjoint
KADID-10K [9]	Synthetic	81	25	10,125	MOS	Reference-disjoint
FLIVE [29]	In-the-wild	–	–	39,808	MOS + patch scores	Official split
SPAQ [44]	In-the-wild	–	–	11,125	MOS	Random 70/10/20

d) *Preprocessing and normalization*: All synthetic datasets in this protocol use the same resizing, cropping, and color normalization pipelines. No statistics from  $D_t$  are computed or applied. In particular, we do not apply target-specific normalization or retune hyperparameters.

e) *Metrics and aggregation*: We report SRCC on raw predictions. For each  $D_s \rightarrow D_t$ , the headline result is the median over the 10 source splits.

f) *Contrast to some prior practice*: Some SSL-IQA works may emphasize within-dataset or mixed-dataset training. Our protocol enforces strict zero-shot transfer  $D_s \rightarrow D_t$  with a fixed encoder and hyperparameters chosen on  $D_s$ , isolating representation quality rather than target adaptation.

## APPENDIX G

### ADDITIONAL T-SNE VISUALIZATIONS

a) *Protocol*: We compute t-SNE [50] on KADID-10K [9] using image-level encoder representations  $\mathbf{H}$  (pre-projector). For each image, we extract features from multiple crops and average them, resulting in 10,125 image-level representations. Before t-SNE, we apply scikit-learn PCA to 50 dimensions with ‘random\_state=123’ and ‘svd\_solver=auto’. We then run 2D t-SNE using scikit-learn TSNE with a fixed seed shared across models: ‘random\_state=123’, ‘perplexity=30’, ‘learning\_rate=200’, ‘n\_iter=2000’, and ‘init=pca’, with default ‘metric=euclidean’ and ‘early\_exaggeration=12.0’. We apply no additional feature normalization before PCA or t-SNE. Unless otherwise noted, the plotted images and t-SNE settings are identical across models; only the extracted representations differ. All visualizations are qualitative diagnostics and are not used for model selection.

b) *Additional visualizations*: Fig. 7 colors the global KADID-10K embedding by severity level and shows that several coarse families exhibit smooth local severity progressions in representation space, even though visually related distortions still overlap. Fig. 8 then focuses on SHAMISA at the subtype level. Blur, compression, and spatial distortions

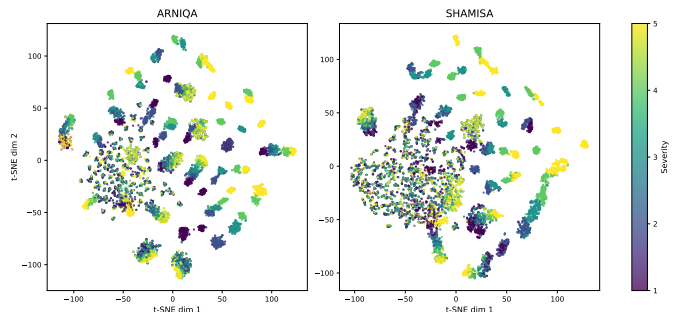


Fig. 7. t-SNE colored by distortion severity on KADID-10K. Colors indicate severity levels 1 to 5 for ARNIQA (left) and SHAMISA (right).

show the clearest subtype-level separation, whereas color and brightness-related manipulations remain more entangled.

## APPENDIX H

### UMAP PROTOCOL DETAILS

We sample 1,000 pristine KADIS images and generate blur-only, noise-only, and blur→noise compositions, with blur applied before noise. The Gaussian blur levels are  $\{0.1, 0.5, 1, 2, 5\}$ , and the white-noise levels are  $\{0.001, 0.002, 0.003, 0.005, 0.01\}$ . For each content image, we generate 5 blur-only samples, 5 noise-only samples, and  $5 \times 5$  blur→noise compositions, for a total of 35k images. We extract  $\mathbf{H}$  using the frozen encoder and the feature-pooling protocol in Sec. IV-B, before the projector head. We apply no feature-wise standardization or  $\ell_2$  normalization to  $\mathbf{H}$  before visualization. We project features to 50 dimensions with scikit-learn PCA (‘random\_state=123’, ‘svd\_solver=auto’). We then fit a 2D UMAP embedding with ‘n\_neighbors=50’, ‘min\_dist=0.99’, ‘metric=euclidean’, ‘init=spectral’, and ‘random\_state=123’, using the same seed and settings across models. For visualization, each point is colored by the relative blur/noise contribution, and its marker opacity increases with normalized total severity.

## APPENDIX I

### GMAD PROTOCOL DETAILS

For each model, we compute scalar quality predictions on the full Waterloo Exploration distorted pool using a frozen encoder and a ridge regressor trained on KADID-10K, following the feature extraction and normalization in Sec. IV-B. For a given defender  $f_{\text{def}}$  and attacker  $f_{\text{att}}$ , we bin all images into  $N_{\text{bins}}=10$  equal-count levels based on  $f_{\text{def}}$  predictions and select the lowest and highest bins. Within each selected

TABLE VI

FULL-REFERENCE IQA COMPARISON ON SYNTHETIC DISTORTION DATASETS. REPORTED ROWS ARE TAKEN FROM PRIOR WORK. SHAMISA-FR USES THE SAME FIXED-ENCODER EVALUATION PROTOCOL AS OUR NR SETTING, AND EACH VALUE IS THE MEDIAN OVER 10 RANDOM SPLITS. BEST AND SECOND-BEST VALUES IN EACH COLUMN ARE SHOWN IN BOLD AND UNDERLINED.

Method	Type	LIVE		CSIQ		TID2013		KADID-10K	
		SRCC	PLCC	SRCC	PLCC	SRCC	PLCC	SRCC	PLCC
PSNR	Traditional	0.881	0.868	0.820	0.824	0.643	0.675	0.677	0.680
SSIM [52]	Traditional	0.921	0.911	0.854	0.835	0.642	0.698	0.641	0.633
FSIM [53]	Traditional	0.964	0.954	0.934	0.919	0.852	0.875	0.854	0.850
VSI [54]	Traditional	0.951	0.940	0.944	0.929	0.902	0.903	0.880	0.878
PieAPP [55]	Deep learning	0.915	0.905	0.900	0.881	0.877	0.850	0.869	0.869
LPIPS [36]	Deep learning	0.932	0.936	0.884	0.906	0.673	0.756	0.721	0.713
DISTS [56]	Deep learning	0.953	0.954	0.942	0.942	0.853	0.873	–	–
DRF-IQA [57]	Deep learning	<b>0.983</b>	<b>0.983</b>	0.964	0.960	<b>0.944</b>	<b>0.942</b>	–	–
CONTRIQUE-FR [17]	SSL + LR	0.966	0.966	0.956	0.964	0.909	0.915	<b>0.946</b>	<b>0.947</b>
Re-IQA-FR [58]	SSL + LR	<u>0.969</u>	<u>0.974</u>	0.961	0.962	<u>0.920</u>	<u>0.921</u>	<u>0.933</u>	<u>0.936</u>
ARNIQA-FR [18]	SSL + LR	<u>0.969</u>	0.972	<b>0.971</b>	<u>0.975</u>	0.898	0.901	0.920	0.919
<b>SHAMISA-FR</b>	SSL + LR	0.962	0.970	<u>0.968</u>	<b>0.982</b>	0.909	0.906	0.899	0.892

TABLE VII

GMAD SUMMARY ON WATERLOO EXPLORATION (DISTORTED POOL) BETWEEN SHAMISA AND ARNIQA. ATTACKER GAP DENOTES THE ATTACKER-SIDE SCORE SEPARATION OF THE SELECTED PAIR WITHIN THE DEFENDER-DEFINED BIN; LOWER IS BETTER.

Defender, Quality Level	Bin size	Top-1 attacker gap
ARNIQA, high	9488	8.2717
ARNIQA, low	9488	8.6782
SHAMISA, high	9488	4.1860
SHAMISA, low	9488	3.1356

bin, we select the top-1 attacker-gap pair, defined as the pair with maximal attacker score separation while remaining in the same defender-defined level, and report it for visualization. All reported figures use the Waterloo distorted subset. Table VII summarizes the corresponding top-1 attacker gaps for the four defender/quality-level cases.

## APPENDIX J ADDITIONAL ABLATIONS

Table VIII reports the complete ablation catalog, including finer-grained graph removals (B2–B5), OT sparsification (C1), the additional distortion-engine setting D3, and severity-dependent edge weighting (F1). Two patterns are worth noting. (1) Single metadata edge removals (B3–B5) each cause only small changes, while metadata-only (B7) remains substantially below A0, indicating metadata relations are individually weak but collectively useful through redundancy and coverage of diverse distortion semantics. (2) Severity-dependent edge weighting is helpful but secondary: replacing  $\phi, \hat{\phi}$  with the identity (F1) reduces  $SRCC_g$  to 0.8736, whereas removing OT alignment (E1) drops to 0.7887, reinforcing that OT-guided global structure is the central mechanism while severity shaping refines it.

TABLE VIII

FULL ABLATION CATALOG. FOR EACH DATASET WE RUN 10 RANDOM SPLITS AND REPORT THE MEDIAN TEST SRCC/PLCC ACROSS SPLITS, THEN AVERAGE WITHIN GROUPS: SYNTHETIC {LIVE, CSIQ, TID2013, KADID-10K}, AUTHENTIC {FLIVE, SPAQ}, AND  $SRCC_g/PLCC_g$  DENOTE THE AVERAGE OVER THE SIX PER-DATASET MEDIAN SRCC/PLCC VALUES.

Variant	$SRCC_g$	$PLCC_g$	$SRCC_a$	$PLCC_a$	$SRCC_s$	$PLCC_s$
<b>A0: SHAMISA</b>	0.8862	0.9042	0.7620	0.8040	0.9483	0.9543
<i>(A) Graph weighting &amp; regularization</i>						
A1: Binary $\mathcal{G}$	0.8767	0.8924	0.7475	0.7821	0.9374	0.9457
A2: No $\mathcal{R}_{\text{graph}}$	0.8813	0.8981	0.7471	0.7908	0.9450	0.9497
A3: No $\Phi$ (fixed linear mixture)	0.8759	0.8951	0.7479	0.7896	0.9361	0.9457
A4: No stop-grad through $\Phi$	0.8797	0.8980	0.7521	0.7950	0.9395	0.9469
<i>(B) Source graph contributions</i>						
B1: No $\mathcal{G}^o$ (OT graph)	0.8600	0.8787	0.7661	0.8069	0.8995	0.9092
B2: No $\mathcal{G}^k$ (kNN graph)	0.8815	0.8989	0.7475	0.7890	0.9452	0.9520
B3: No $\mathcal{G}^{r,d}$ (ref-dist metadata)	0.8765	0.8931	0.7484	0.7865	0.9366	0.9443
B4: No $\mathcal{G}^{d,d}$ (dist-dist metadata)	0.8771	0.8937	0.7494	0.7867	0.9370	0.9451
B5: No $\mathcal{G}^{r,r}$ (ref-ref metadata)	0.8814	0.8976	0.7462	0.7854	0.9458	0.9520
B6: $\mathcal{G}^k$ only	0.7891	0.8018	0.7577	0.7825	0.7922	0.8017
B7: Metadata only $\{\mathcal{G}^{r,d}, \mathcal{G}^{d,d}, \mathcal{G}^{r,r}\}$	0.8467	0.8648	0.7634	0.8010	0.8801	0.8905
B8: Structure only $\{\mathcal{G}^k, \mathcal{G}^o\}$	0.8753	0.8961	0.7419	0.7891	0.9387	0.9475
<i>(C) Sparsity operators &amp; topology shaping</i>						
C1: Row-wise Top- $k$ in $\mathcal{G}^o$ ( $k=8$ )	0.8734	0.8898	0.7500	0.7918	0.9307	0.9359
<i>(D) Distortion engine</i>						
D1: $M_d=1$	0.8775	0.9077	0.7259	0.7684	0.9519	0.9783
D2: Discrete severities ( $L=5$ )	0.8767	0.8987	0.7456	0.7890	0.9386	0.9518
D3: Uniform severity sampling	0.8743	0.8955	0.7439	0.7946	0.9359	0.9432
D4: Fixed composition order $\pi$	0.8587	0.8712	0.7434	0.7668	0.9113	0.9215
<i>(E) Objective form &amp; diagnostics</i>						
E1: No $\mathcal{L}_{\text{ot}}$	0.7887	0.8009	0.7597	0.7836	0.7904	0.7996
<i>(F) Severity mapping diagnostics</i>						
F1: Identity $\phi, \hat{\phi}$	0.8736	0.8937	0.7459	0.7914	0.9335	0.9423

## APPENDIX K ADDITIONAL PRE-TRAINING DYNAMICS

### A. Downstream SRCC During SSL Pre-Training

We track downstream SRCC of the frozen pre-trained encoder across pre-training snapshots using the same lightweight regressor as in the main experiments. Fig. 5 complements the main text by showing that SRCC improves rapidly in the early phase and then largely saturates across datasets, while the final checkpoint is not uniformly optimal for every dataset. This

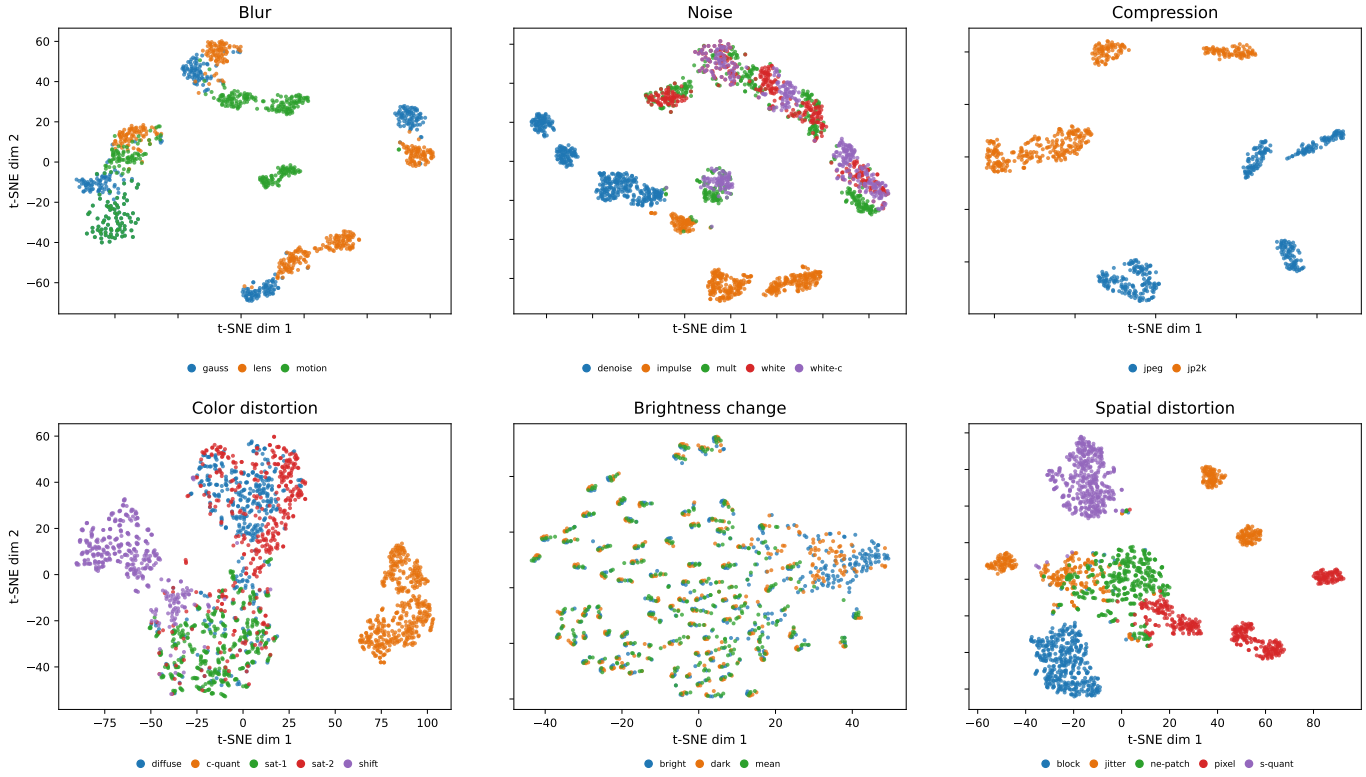


Fig. 8. Subtype-colored t-SNE views for SHAMISA, including six KADID-10K distortion families.

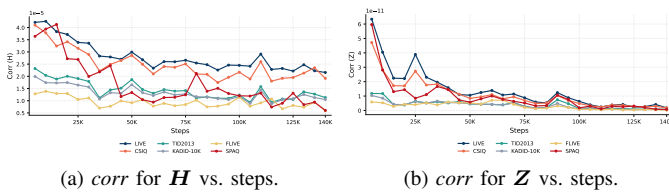


Fig. 9. Feature decorrelation proxy (*corr*) over SSL pre-training. Both  $H$  and  $Z$  show a rapid early drop followed by stabilization, consistent with progressively reduced redundancy across feature dimensions.

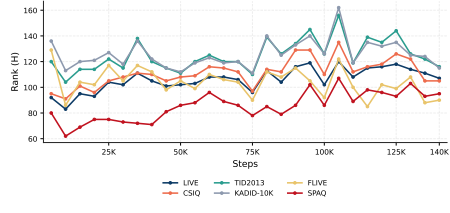


Fig. 10. Effective dimensionality proxy (*rank*) for  $H$  over SSL pre-training. The encoder representation uses a substantial number of active dimensions throughout training and then stabilizes after the early phase.

figure serves as a compact convergence record rather than a separate endpoint-results table.

### B. Encoder Representations and Projector Embeddings During SSL Pre-Training

We additionally track correlation and invariance for both encoder representations  $H$  and projector embeddings  $Z$ , together with rank for  $H$ , during SSL pre-training. Fig. 9 shows that the correlation proxy drops quickly and then stabilizes for both  $H$  and  $Z$ , consistent with progressively reduced feature redundancy. Fig. 10 shows that the effective dimensionality of  $H$  evolves during training and then settles after the early phase, while Fig. 11 shows a similar decrease and stabilization in the invariance proxy.

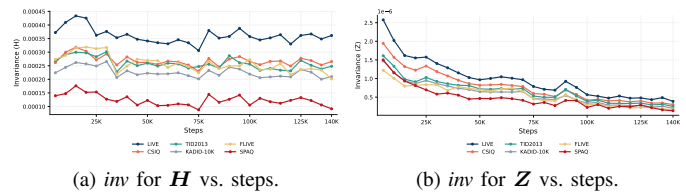


Fig. 11. Invariance proxy (*inv*) over SSL pre-training. Curves generally decrease and then stabilize, consistent with paired views becoming closer in representation space as training proceeds.

all others fixed. Table IX summarizes SRCC sensitivity on LIVE, CSIQ, TID2013, KADID-10K, FLIVE, and SPAQ. For each hyperparameter,  $\Delta$  is the largest minus smallest SRCC across the sweep. Larger  $\Delta$  indicates higher sensitivity.

## APPENDIX L

### HYPERPARAMETER SENSITIVITY DETAILS

We perform one-at-a-time sweeps around the A0 reference configuration, varying a single hyperparameter while keeping

## REFERENCES

[1] X. Wang, L. Xie, C. Dong, and Y. Shan, “Real-ESRGAN: Training real-world blind super-resolution with pure synthetic data,” in *Proceedings of the IEEE/CVF international conference on computer vision*, 2021, pp. 1905–1914.

TABLE IX

**SENSITIVITY SUMMARY FOR SRCC.** FOR EACH HYPERPARAMETER,  $\Delta$  IS THE LARGEST MINUS SMALLEST SRCC ACROSS THE SWEEP. LARGER  $\Delta$  INDICATES HIGHER SENSITIVITY. THE MOST SENSITIVE AND SECOND MOST SENSITIVE HYPERPARAMETERS PER DATASET ARE SHOWN IN **BOLD** AND UNDERLINED.

HP	LIVE	CSIQ	TID2013	KADID-10K	FLIVE	SPAQ	Mean
$d_h$	0.012	0.003	0.003	0.006	0.004	<b>0.007</b>	0.006
$d_z$	0.006	0.002	0.002	0.000	0.003	<u>0.007</u>	0.003
$B$	0.002	0.001	0.003	0.005	0.001	0.001	0.002
$k_n$	0.007	0.009	0.006	0.016	0.007	0.001	0.008
$K$	<u>0.019</u>	0.035	0.061	0.030	0.007	0.005	0.026
$\gamma$	0.017	<u>0.045</u>	<u>0.089</u>	<u>0.070</u>	<u>0.033</u>	0.001	<u>0.042</u>
$\alpha$	0.003	0.004	0.006	0.010	0.003	0.001	0.004
$\beta$	0.005	0.004	0.006	0.005	0.007	0.003	0.005
$\xi$	0.010	0.002	0.003	0.013	0.000	0.000	0.005
$\eta$	<b>0.054</b>	<b>0.096</b>	<b>0.208</b>	<b>0.226</b>	<b>0.035</b>	0.001	<b>0.104</b>

- [2] T.-Y. Chiu, Y. Zhao, and D. Gurari, "Assessing image quality issues for real-world problems," in *proceedings of the IEEE/CVF conference on computer vision and pattern recognition*, 2020, pp. 3646–3656.
- [3] L. Agnolucci, L. Galteri, M. Bertini, and A. Del Bimbo, "Perceptual quality improvement in videoconferencing using keyframes-based gan," *IEEE Transactions on Multimedia*, 2023.
- [4] A. C. Bovik, "Automatic prediction of perceptual image and video quality," *Proceedings of the IEEE*, vol. 101, pp. 2008–2024, 2013.
- [5] Z. Wang and A. C. Bovik, "Mean squared error: Love it or leave it? a new look at signal fidelity measures," *IEEE Signal Processing Magazine*, vol. 26, no. 1, pp. 98–117, 2009.
- [6] W. Zhang, K. Ma, J. Yan, D. Deng, and Z. Wang, "Blind image quality assessment using a deep bilinear convolutional neural network," *IEEE Transactions on Circuits and Systems for Video Technology*, vol. 30, no. 1, pp. 36–47, 2018.
- [7] S. Su, Q. Yan, Y. Zhu, C. Zhang, X. Ge, J. Sun, and Y. Zhang, "Blindly assess image quality in the wild guided by a self-adaptive hyper network," in *Proc. IEEE Conf. Comput. Vision Pattern Recognit.*, 2020, pp. 3667–3676.
- [8] S. A. Golestaneh, S. Dadsetan, and K. M. Kitani, "No-reference image quality assessment via transformers, relative ranking, and self-consistency," in *Proceedings of the IEEE/CVF Winter Conference on Applications of Computer Vision*, 2022, pp. 1220–1230.
- [9] H. Lin, V. Hosu, and D. Saupe, "Kadid-10k: A large-scale artificially distorted iqa database," in *2019 Tenth International Conference on Quality of Multimedia Experience (QoMEX)*. IEEE, 2019, pp. 1–3.
- [10] K. Zhao, K. Yuan, M. Sun, M. Li, and X. Wen, "Quality-aware pre-trained models for blind image quality assessment," in *Proceedings of the IEEE/CVF Conference on Computer Vision and Pattern Recognition*, 2023, pp. 22 302–22 313.
- [11] A. Saha, S. Mishra, and A. C. Bovik, "Re-iqa: Unsupervised learning for image quality assessment in the wild," in *Proceedings of the IEEE/CVF Conference on Computer Vision and Pattern Recognition*, 2023, pp. 5846–5855.
- [12] T. Chen, S. Kornblith, M. Norouzi, and G. Hinton, "A simple framework for contrastive learning of visual representations," in *International conference on machine learning*. PMLR, 2020, pp. 1597–1607.
- [13] K. He, H. Fan, Y. Wu, S. Xie, and R. Girshick, "Momentum contrast for unsupervised visual representation learning," in *Proceedings of the IEEE/CVF conference on computer vision and pattern recognition*, 2020, pp. 9729–9738.
- [14] P. Biela, T. Kajdanowicz, and N. V. Chawla, "Graph barlow twins: A self-supervised representation learning framework for graphs," *arXiv preprint arXiv:2106.02466*, 2021.
- [15] C.-Y. Chuang, J. Robinson, Y.-C. Lin, A. Torralba, and S. Jegelka, "Debiased contrastive learning," in *Advances in Neural Information Processing Systems*, 2020.
- [16] T.-S. Chen, W.-C. Hung, H.-Y. Tseng, S.-Y. Chien, and M.-H. Yang, "Incremental false negative detection for contrastive learning," in *International Conference on Learning Representations*, 2022.
- [17] P. C. Madhusudana, N. Birkbeck, Y. Wang, B. Adsumilli, and A. C. Bovik, "Image quality assessment using contrastive learning," *IEEE Transactions on Image Processing*, vol. 31, pp. 4149–4161, 2022.
- [18] L. Agnolucci, L. Galteri, M. Bertini, and A. Del Bimbo, "Arniqa: Learning distortion manifold for image quality assessment," in *Proceedings of the IEEE/CVF Winter Conference on Applications of Computer Vision*, 2024, pp. 189–198.
- [19] M. Naseri and M. Biparva, "Exgrg: Explicitly-generated relation graph for self-supervised representation learning," *arXiv preprint arXiv:2402.06737*, 2024.
- [20] A. Mittal, A. K. Moorthy, and A. C. Bovik, "No-reference image quality assessment in the spatial domain," *IEEE Transactions on image processing*, vol. 21, no. 12, pp. 4695–4708, 2012.
- [21] A. Mittal, R. Soundararajan, and A. C. Bovik, "Making a "completely blind" image quality analyzer," *IEEE Signal processing letters*, vol. 20, no. 3, pp. 209–212, 2012.
- [22] A. K. Moorthy and A. C. Bovik, "Blind image quality assessment: From natural scene statistics to perceptual quality," *IEEE transactions on Image Processing*, vol. 20, no. 12, pp. 3350–3364, 2011.
- [23] M. A. Saad, A. C. Bovik, and C. Charrier, "Blind image quality assessment: A natural scene statistics approach in the dct domain," *IEEE transactions on Image Processing*, vol. 21, no. 8, pp. 3339–3352, 2012.
- [24] P. Ye, J. Kumar, L. Kang, and D. Doermann, "Unsupervised feature learning framework for no-reference image quality assessment," in *2012 IEEE conference on computer vision and pattern recognition*. IEEE, 2012, pp. 1098–1105.
- [25] J. Xu, P. Ye, Q. Li, H. Du, Y. Liu, and D. Doermann, "Blind image quality assessment based on high order statistics aggregation," *IEEE Transactions on Image Processing*, vol. 25, no. 9, pp. 4444–4457, 2016.
- [26] K. He, X. Zhang, S. Ren, and J. Sun, "Deep residual learning for image recognition," in *Proceedings of the IEEE conference on computer vision and pattern recognition*, 2016, pp. 770–778.
- [27] Z. Tu, X. Yu, Y. Wang, N. Birkbeck, B. Adsumilli, and A. C. Bovik, "Rapique: Rapid and accurate video quality prediction of user generated content," *IEEE Open Journal of Signal Processing*, vol. 2, pp. 425–440, 2021.
- [28] J. Ke, Q. Wang, Y. Wang, P. Milanfar, and F. Yang, "MUSIQ: multi-scale image quality transformer," *CoRR*, vol. abs/2108.05997, 2021. [Online]. Available: <https://arxiv.org/abs/2108.05997>
- [29] Z. Ying, H. Niu, P. Gupta, D. Mahajan, D. Ghadiyaram, and A. C. Bovik, "From patches to pictures (paq-2-piq): Mapping the perceptual space of picture quality," *CoRR*, vol. abs/1912.10088, 2019. [Online]. Available: <http://arxiv.org/abs/1912.10088>
- [30] H. Zeng, L. Zhang, and A. C. Bovik, "A probabilistic quality representation approach to deep blind image quality prediction," *arXiv preprint arXiv:1708.08190*, 2017.
- [31] A. Bardes, J. Ponce, and Y. LeCun, "Vicreg: Variance-invariance-covariance regularization for self-supervised learning," *arXiv preprint arXiv:2105.04906*, 2021.
- [32] P. Mohammadi, A. Ebrahimi-Moghadam, and S. Shirani, "Subjective and objective quality assessment of image: A survey," *arXiv preprint arXiv:1406.7799*, 2014.
- [33] D. M. Chandler, "Seven challenges in image quality assessment: past, present, and future research," *International Scholarly Research Notices*, vol. 2013, no. 1, p. 905685, 2013.
- [34] R. Balestriero and Y. LeCun, "Contrastive and non-contrastive self-supervised learning recover global and local spectral embedding methods," *arXiv preprint arXiv:2205.11508*, 2022.
- [35] X. Chen and K. He, "Exploring simple siamese representation learning," in *Proceedings of the IEEE/CVF conference on computer vision and pattern recognition*, 2021, pp. 15 750–15 758.
- [36] R. Zhang, P. Isola, A. A. Efros, E. Shechtman, and O. Wang, "The unreasonable effectiveness of deep features as a perceptual metric," in *Proceedings of the IEEE conference on computer vision and pattern recognition*, 2018, pp. 586–595.
- [37] M. Cuturi, "Sinkhorn distances: Lightspeed computation of optimal transport," *Advances in neural information processing systems*, vol. 26, 2013.
- [38] Y. M. Asano, C. Rupprecht, and A. Vedaldi, "Self-labelling via simultaneous clustering and representation learning," *arXiv preprint arXiv:1911.05371*, 2019.
- [39] M. Caron, I. Misra, J. Mairal, P. Goyal, P. Bojanowski, and A. Joulin, "Unsupervised learning of visual features by contrasting cluster assignments," *Advances in neural information processing systems*, vol. 33, pp. 9912–9924, 2020.
- [40] D. Ha, A. Dai, and Q. V. Le, "Hypernetworks," 2016.
- [41] H. R. Sheikh, M. F. Sabir, and A. C. Bovik, "A statistical evaluation of recent full reference image quality assessment algorithms," *IEEE Transactions on image processing*, vol. 15, no. 11, pp. 3440–3451, 2006.

- [42] E. C. Larson and D. M. Chandler, "Most apparent distortion: full-reference image quality assessment and the role of strategy," *Journal of electronic imaging*, vol. 19, no. 1, p. 011006, 2010.
- [43] N. Ponomarenko, O. Ieremeiev, V. Lukin, K. Egiazarian, L. Jin, J. Astola, B. Vozel, K. Chehdi, M. Carli, F. Battisti *et al.*, "Color image database tid2013: Peculiarities and preliminary results," in *European workshop on visual information processing (EUVIP)*. IEEE, 2013, pp. 106–111.
- [44] Y. Fang, H. Zhu, Y. Zeng, K. Ma, and Z. Wang, "Perceptual quality assessment of smartphone photography," in *Proceedings of the IEEE/CVF Conference on Computer Vision and Pattern Recognition*, 2020, pp. 3677–3686.
- [45] A. E. Hoerl and R. W. Kennard, "Ridge regression: Biased estimation for nonorthogonal problems," *Technometrics*, vol. 12, no. 1, pp. 55–67, 1970.
- [46] VQEG, "Final report from the video quality experts group on the validation of objective quality metrics for video quality assessment," 2000.
- [47] S. Su, Q. Yan, Y. Zhu, J. Sun, and Y. Zhang, "From distortion manifold to perceptual quality: a data efficient blind image quality assessment approach," *Pattern Recognition*, vol. 133, p. 109047, 2023.
- [48] K. Ma, Q. Wu, Z. Wang, Z. Duanmu, H. Yong, H. Li, and L. Zhang, "Group mad competition—a new methodology to compare objective image quality models," in *Proceedings of the IEEE Conference on Computer Vision and Pattern Recognition*, 2016, pp. 1664–1673.
- [49] K. Ma, Z. Duanmu, Q. Wu, Z. Wang, H. Yong, H. Li, and L. Zhang, "Waterloo exploration database: New challenges for image quality assessment models," *IEEE Transactions on Image Processing*, vol. 26, no. 2, pp. 1004–1016, 2016.
- [50] L. Van der Maaten and G. Hinton, "Visualizing data using t-sne." *Journal of machine learning research*, vol. 9, no. 11, 2008.
- [51] L. McInnes, J. Healy, and J. Melville, "Umap: Uniform manifold approximation and projection for dimension reduction," *arXiv preprint arXiv:1802.03426*, 2018.
- [52] Z. Wang, A. C. Bovik, H. R. Sheikh, and E. P. Simoncelli, "Image quality assessment: from error visibility to structural similarity," *IEEE Trans. Image Process.*, vol. 13, no. 4, pp. 600–612, April 2004.
- [53] L. Zhang, L. Zhang, X. Mou, and D. Zhang, "FSIM: A feature similarity index for image quality assessment," *IEEE Trans. Image Process.*, vol. 20, no. 8, pp. 2378–2386, 2011.
- [54] L. Zhang, Y. Shen, and H. Li, "VSI: A visual saliency-induced index for perceptual image quality assessment," *IEEE Trans. Image Process.*, vol. 23, no. 10, pp. 4270–4281, 2014.
- [55] E. Prashnani, H. Cai, Y. Mostofi, and P. Sen, "Pieapp: Perceptual image-error assessment through pairwise preference," in *Proc. IEEE Conf. Comput. Vision Pattern Recognit.*, 2018, pp. 1808–1817.
- [56] K. Ding, K. Ma, S. Wang, and E. P. Simoncelli, "Image quality assessment: Unifying structure and texture similarity," *IEEE Trans. Pattern Anal. Mach. Intell.*, pp. 1–1, 2020.
- [57] W. Kim, A.-D. Nguyen, S. Lee, and A. C. Bovik, "Dynamic receptive field generation for full-reference image quality assessment," *IEEE Trans. Image Process.*, vol. 29, pp. 4219–4231, 2020.
- [58] A. Saha, S. Mishra, and A. C. Bovik, "Re-iqa: Unsupervised learning for image quality assessment in the wild," in *2023 IEEE/CVF Conference on Computer Vision and Pattern Recognition (CVPR)*. IEEE, 2023, pp. 5846–5855.